Article

Revealing the Magmatic Impulse Emplacement and Evolution Path of Kimberlite in Southern Liaoning through Mineralogical Characteristics of the Phlogopite Zone

Sishun Ma [1,*], Ende Wang [1,*] and Haitao Fu [2]

[1] School of Resources and Civil Engineering, Northeastern University, Shenyang 110819, China
[2] Liaoning Geological Exploration Mining Group, Shenyang 110032, China; lnfht@163.com
* Correspondence: masishun@stumail.neu.edu.cn (S.M.); wnd@mail.neu.edu.cn (E.W.)

Abstract: Phlogopite is a crucial indicator for effectively constraining the magmatic evolution and emplacement mechanism of kimberlite. In this study, samples were collected from the No. 110 kimberlite pipe within diamond belt I and the No. 50 kimberlite pipe within diamond belt II in the southern Liaoning diamond mining area in the eastern North China Craton (NCC). Zonation is highly developed in the phlogopite; the major and trace element compositions of the phlogopite zonation in the samples were analyzed. In this study, phlogopite from the No. 50 pipe kimberlite (#50 phlogopite) zonation is divided into the following components: (1) The cores, low Ti-Cr xenocryst, average $Mg^{\#} = 90.6$, has a resorption structure, the presence of serpentine and talc minerals in low Ti-Cr cores (xenocrysts) can be used as evidence for hydrothermal metasomatism; (2) cores/inner rims (between core and outer rim), high Ti-Cr, it is thought to be related to the assimilation of mantle materials by deep kimberlite magma, average $Mg^{\#} = 88.2$; (3) outer rims, low-Cr/Cr-poor, average $Mg^{\#} = 82.4$, Fe, Al and Ba contents increased, and there was a trend of evolution to biotite composition believed to be related to the metasomatic metamorphism of melt and wall rock during the late magmatic evolution or ascent; (4) rinds, it is characterized by re-enrichment of Mg, rind I (low-Ti-Cr, average $Mg^{\#} = 88.4$), rind II (high-Ti-Cr, $Mg^{\#} = 88.6$), rind II may be formed earlier than rind I. Rind is very rare and has been reported for the first time in southern Liaoning kimberlite. This study was only accidentally found in the outermost part of #50 phlogopite, the Mg-rich feature represents an environment in which oxygen fugacity has increased. The phlogopite in samples from pipe No. 110 (#110 phlogopite) exhibits relatively homogeneous characteristics across different zones and is more enriched in Al and Ba, which is likely the result of mantle metasomatism. Due to its euhedral characteristics and limited composition variation, it is considered that #110 phlogopite is more likely to be derived from direct crystallization from magma than from xenocrysts. In addition, based on the simultaneous enrichment of Al and Fe in phlogopite from the core to the outer rim, pipe No. 50 was determined to be a micaceous kimberlite, while pipe No. 110 more closely resembles group I kimberlites. This paper proposes that successive pulses of kimberlite magma emplacement gradually metasomatized the conduit, and subsequent kimberlite magma ascended along the metasomatized conduit, thereby minimizing the interaction between the later magma and the surrounding mantle lithosphere.

Keywords: phlogopite zone of kimberlite; magmatic evolution; emplacement mechanism

1. Introduction

The primary host rocks for diamonds worldwide are broadly classified into two categories: kimberlites and lamproites. The key difference between kimberlites and lamproites is that the former are either sourced in the asthenosphere or formed from subcratonic lithospheric mantle (SCLM) lithologies metasomatized by asthenospheric melts shortly before partial melting [1–5], whereas the latter are purely SCLM melts from metasomatized lithologies [6–8]. Kimberlites, a rare ultrabasic volcanic rock, are considered one of the

primary host rocks of diamonds and may represent magmas originating from the deepest parts of the mantle (>150–200 km) that have been observed on the Earth's surface [9]. Kimberlites have significant economic and scientific importance due to their role as primary diamond hosts and potential representatives of the deepest continental magmas. At the surface, kimberlites manifest in the form of diatremes, sills, and dikes. Kimberlite diatremes typically consist of multiple units derived from distinct magma batches, whereas sills and dikes represent one or more discrete magma injections at the Earth's surface [10–14]. Kimberlites entrain large amounts of mantle and crustal material (xenoliths and xenocrysts), including fragments of previously failed kimberlite deposits, and these xenoliths and xenocrysts contain much information about the deep Earth, providing a valuable way to study the deep Earth. Hence, the significance of kimberlite research cannot be underestimated, and it is imperative to investigate the compositions, magma evolution and emplacement mechanisms of kimberlites.

The magmatic evolution path and emplacement process of the southern Liaoning kimberlite located in the eastern part of the North China Craton (NCC) have not been effectively discussed. In the past, it was believed that the exsolution of significant amounts of CO_2-rich phases in the deep mantle served as the primary driving force for kimberlite melt emplacement. The presence of a significant quantity of carbonates in the kimberlite matrix clearly contradicts this viewpoint [15–19]. We have identified a significant quantity of carbonate veins and minerals (primarily calcite) within the southern Liaoning kimberlite deposits and an abundance of nonexplosively emplaced kimberlites (such as the No. 110 kimberlite dike). Therefore, there is an urgent need to find a suitable method and media to study this problem.

Phlogopite is a rock-forming mineral commonly found in ultramafic–alkaline mantle-derived rocks, such as kimberlites, aillikites, orangeites and carbonatites [20–22]. Phlogopite exists as megacrysts (>10 mm) [14], macrocrysts (~>0.5 mm), and groundmass grains (~<0.1 mm) [21,23–27]. These crystals often show complex zonation, with dark-colored overgrowths often formed as rims around cores with resorption structures. Deformation structures, such as kink-banding and undulose extinction, are commonly observed and are believed to result from deep mantle transport. Additionally, some of the phlogopite macrocrysts likely originate from metasomatized mantle rock disaggregation. It has been reported that the composition of phlogopite macrocryst cores in the Wesselton kimberlite (Kimberley cluster) is similar to that of phlogopite in the Kimberley metasomatic mantle rocks [28], suggesting that the two may have similar origins. The intricate zoning pattern of phlogopite has immense potential to unravel the crust–mantle evolution of kimberlite, providing a rare opportunity to study the evolution of kimberlite and its related melts after olivine.

Worldwide, over the last few decades, much information about the magma evolution and lithology determination of kimberlites has been gleaned from the zonal structure of olivine elsewhere in the past [2,29–36]. Currently, global research on minerals in kimberlite primarily focuses on olivine, garnet, perovskite, and spinel [37–46]. The olivine found in southern Liaoning's kimberlite typically exhibits pronounced serpentinization, posing challenges for comprehensive investigation. Therefore, this study focuses on phlogopite as one of the minerals that effectively preserves records of fluid migration and magmatism in both the mantle and crust. Phlogopite serves as a valuable petrogenetic indicator for tracing the evolutionary processes of kimberlite magma. Additionally, the compositional analysis of phlogopite can be utilized to classify ultramafic–alkaline volcanic rocks. Therefore, awareness of the composition of the phlogopite zone is crucial for understanding the emplacement process and evolution of enigmatic kimberlite magmas. Numerous studies on cratonic xenoliths, such as kimberlites and related rocks, have demonstrated that phlogopite is a valuable indicator mineral for deciphering mantle metasomatism and magmatic evolution processes in the SCLM [47–54].

Despite being a prevalent mineral in kimberlites, limited petrographic and compositional information is available about phlogopite in southern Liaoning kimberlite. During

the study, the remarkably narrow outermost rinds of phlogopite in the southern Liaoning kimberlite were newly discovered and classified based on their compositional characteristics into low-Ti-Cr rinds (rind I) and high-Ti-Cr rinds (rind II). This has allowed us to uncover the complex history of phlogopite crystal growth stages and multistage magmatic emplacement events.

2. Geological Setting

The North China Craton (NCC) is the largest and oldest craton in China, and the diamond mining area in southern Liaoning is located in the eastern NCC, which is the oldest tectonic unit in China with crustal components up to 3.8 Ga. The NCC was stable until early Paleozoic kimberlite magmatism took place [41]. The NCC is bounded by the late Paleozoic Central Asian Orogenic Belt in the north, the early Paleozoic Qilianshan Orogen in the west and the Qinling–Dabie–Sulu ultrahigh-pressure metamorphic belt in the south, which separates the NCC from the South China Block (Figure 1a). The wall rocks intruded by kimberlites in the Wafangdian region comprise an Archean–Paleoproterozoic basement named the Liaohe Group, which consists of amphibolite and gneiss, and a Neoproterozoic cover named the Qingbaikou Formation, which consists of limestone, shale, and sandstone. A few Ordovician limestone rocks also occur as wall rocks [40].
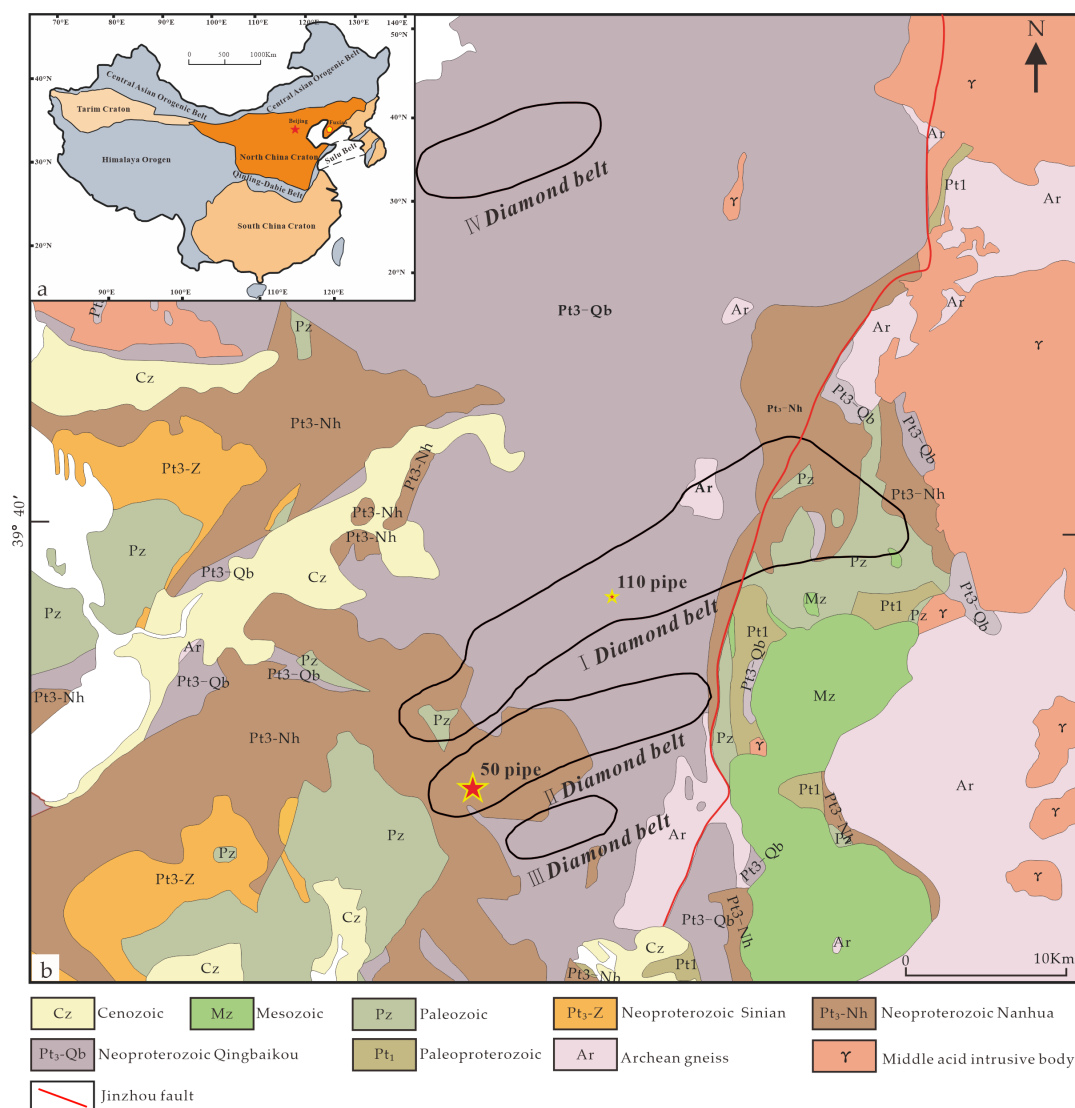

Figure 1. Simplified geologic map showing the cratons in China (**a**) and simplified geologic map of the diamondiferous Wafangdian region (**b**) (modified after [55]).

The kimberlite clusters in southern Liaoning have belt-like distributions. According to the arrangement and association of clusters, the region can be divided into four nearly parallel kimberlite diamond belts that are oriented northeast–southwest. The kimberlite samples in this study are from the No. 110 pipe in the No. I diamond belt and the No. 50 pipe in the No. II diamond belt in southern Liaoning (Figure 1b). The pipes in this area are often carrot-like in shape and are vertical. According to the actual investigation situation, the No. II diamond belt has a higher diamond grade and better economic value than the other belts and contains No. 50 pipe.

3. Analytical Methods

3.1. Electron Probe Micro-Analysis of Phlogopite

Electron probe microanalysis (EPMA) of phlogopite grains was carried out on polished-thin sections. The major compositions of phlogopite were determined by Nanjing Hongchuang Geological Exploration Technology Service Co., Ltd. (Nanjing, China) using a JEOL JXA-iSP100 electron probe microanalyzer. The background counting time was half the peak at the high and low background positions. All of the data were corrected using the ZAF correction method for the matrix effect.

The accelerating voltage, beam current and beam diameter of the phlogopite analyses were 15 kV, 10 nA and 10 µm, respectively. The counting times per analysis were 10 s on peak positions and 5 s on two background positions located on either side of the peak position. The following standards were used: albite (Na_2O), diopside (SiO_2), almandine (Al_2O_3), olivine (MgO), tugtupite (Cl), orthoclase (K_2O), diopside (CaO), nickel (NiO), hematite (FeO), rhodonite (MnO), chromium (Cr_2O_3), rutile (TiO_2), and barite (BaO).

3.2. X-ray Mapping of Phlogopite

X-ray mapping of phlogopite macrocrysts was undertaken using a JEOL JXA-iSP100 Electron Probe Microanalyzer at Nanjing Hongchuang Geological Exploration Technology Service Co., Ltd. X-ray elemental maps were acquired using a beam voltage of 15 kV, a pixel dwell time between 30 and 102 ms, and a total scanning time between 30 and 45 min for each map.

3.3. LA–ICP–MS Analysis of Phlogopite

In situ trace element analysis of the phlogopite was carried out using thin sections on epoxy mounts using a laser ablation inductively coupled mass spectrometer (LA-ICP–MS) at Nanjing Hongchuang Geological Exploration Technology Service Co., Ltd. The Resolution SE model laser ablation system (Applied Spectra, West Sacramento, USA) was equipped with an ATL (ATLEX 300) excimer laser and a Two Volume S155 ablation cell. The laser ablation system was coupled to an Agilent 7900 ICPMS (Agilent, Santa Clara, CA, USA).

LA–ICP–MS tuning was performed using a 50-micron diameter line scan at 3 µm/s on NIST 612 at ~3.5 J/cm^2 with a repetition rate of 10 Hz. The gas flow was adjusted to obtain the highest sensitivity (^{238}U~6 × 105 cps) and the lowest oxide ratio (ThO/Th < 0.2%). P/A calibration was conducted on NIST 610 using a 100-micron diameter line scan. The other laser parameters are the same as those used for tuning. The masses analyzed were ^7Li, ^9Be, ^{11}B, ^{23}Na, ^{25}Mg, ^{27}Al, ^{29}Si, ^{31}P, ^{34}S, ^{39}K, ^{43}Ca, ^{45}Sc, ^{49}Ti, ^{51}V, ^{53}Cr, ^{55}Mn, ^{57}Fe, ^{59}Co, ^{60}Ni, ^{63}Cu, ^{66}Zn, ^{71}Ga, ^{73}Ge, ^{75}As, ^{85}Rb, ^{88}Sr, ^{89}Y, ^{90}Zr, ^{93}Nb, ^{95}Mo, ^{111}Cd, ^{115}In, ^{118}Sn, ^{121}Sb, ^{133}Cs, ^{137}Ba, ^{139}La, ^{140}Ce, ^{141}Pr, ^{146}Nd, ^{147}Sm, ^{151}Eu, ^{157}Gd, ^{159}Tb, ^{163}Dy, ^{165}Ho, ^{166}Er, ^{169}Tm, ^{173}Yb, ^{175}Lu, ^{178}Hf, ^{181}Ta, ^{182}W, ^{197}Au, ^{205}Tl, ^{208}Pb, ^{209}Bi, ^{232}Th and ^{238}U, with a total sweep time of ~0.34 s. Preablation was conducted for each spot analysis using five laser shots (~0.3 µm in depth) to remove potential surface contamination. The analysis was performed using a 38 µm diameter spot at 5 Hz with a fluence of 3 J/cm^2 [56].

The Iolite software package was used for data reduction [57]. NIST 610 and ^{29}Si were used to calibrate the trace element concentrations as an external reference material and

internal standard element, respectively. The internal standard content of the sample was the value obtained from the EPMA data.

4. Petrography

Fresh kimberlites typically exhibit grayish-green and dark green colors (Figure 2). After weathering, serpentinization and carbonization often occur, resulting in the manifestation of yellowish-brown and earth-yellow colors. A distinct boundary between the xenoliths and the kimberlites can be observed under the microscope (Figure 2C). The xenoliths can be classified into two types: homologous and heterologous [58]. The homologous xenoliths are early kimberlite fragments that have been preserved within the mantle. These fragments typically exhibit a rounded shape and demonstrate the exceptional resorption and transport capabilities of kimberlite magma. The heterologous xenoliths are usually crustal rocks (including limestone and sandstone). The primary minerals of the kimberlite samples are olivine (in pseudomorph form), followed by phlogopite, garnet, pyroxene, and accessory minerals, including perovskite, magnetite, spinel, and apatite. As one of the common rock-forming minerals in kimberlite, phlogopite generally accounts for 1–20% of kimberlite [58]. The concentric zonation structure of phlogopite in the southern Liaoning kimberlites is highly developed (Table 1), and the complex zonation pattern is evident in both back-scattered electron (BSE) images and X-ray elemental maps (Figures 3–5). Based on observations, phlogopite is present in the form of macrocrystals (0.3–0.5 mm for the longest axis of phlogopite), microcrystals (0.2–0.3 mm) and groundmass grains (<0.2 mm) [9]. The macrocrystals and microcrystals of phlogopite typically exhibit anhedral to subhedral morphologies. When observed under a microscope, the phlogopite found in the kimberlite deposits in southern Liaoning appears brownish-yellow with pronounced pleochroism and predominantly occurs as xenocrysts, phenocrysts, and groundmass grains.
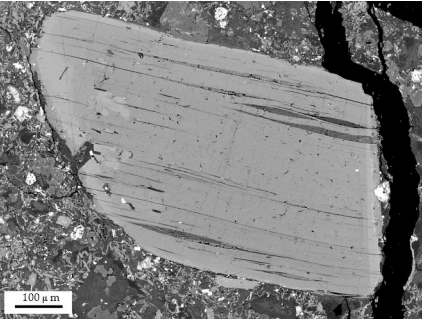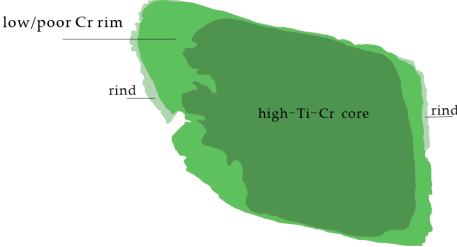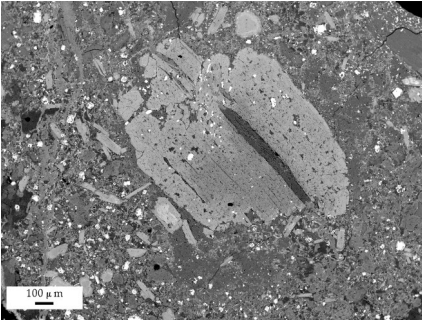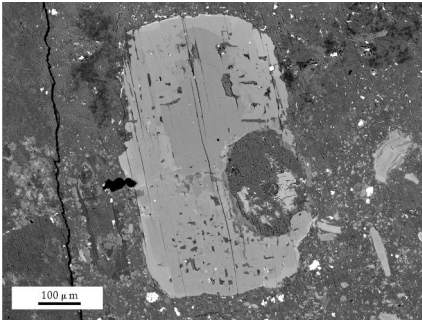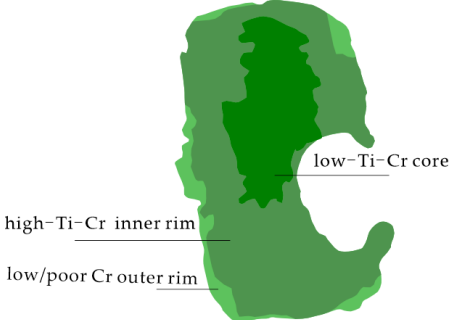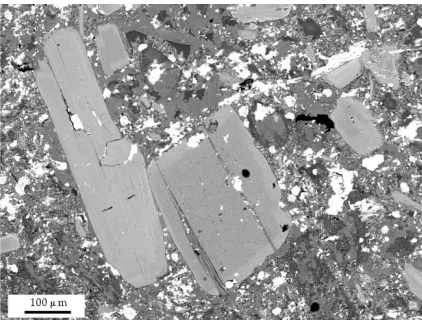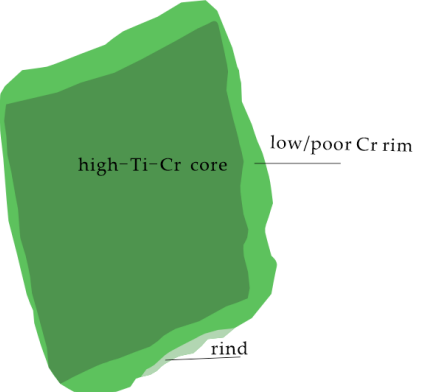
4.1. Petrography of #50 Phlogopite

Phlogopite cores with rounded or embayed outlines often exhibit evidence of resorption and have been subsequently overgrown by one or more zones characterized by distinct compositions. The zones are commonly classified into cores, inner rims, outer rims and rinds, which may not always coexist within a crystal. Rinds are not easily observable due to their narrowness and existence as the outermost layer of crystals. The partially resorbed cores host inclusions of serpentine and talc (Figures 3 and 4a), while mineral inclusions such as apatite and spinel crystals are often observed embedded in the overgrowth layers (such as the inner and outer rims) of phlogopite. Occasionally, kink-banding is observed, which is a characteristic resulting from the processes of magma resorption and transport.

4.2. Petrography of #110 Phlogopite

The No. 110 pipe kimberlite contains a population of euhedral–subhedral phlogopite phenocrysts (#110 phlogopite, usually >150 μm). These grains are in the form of laths, and serpentinization often occurs along the cleavage. Furthermore, the sample matrix in pipe No. 110 exhibits a high concentration of spinel. Apatite commonly occurs in close association with phlogopite, which indicates a strong correlation between the two minerals. The #110 phlogopite often exhibits a high degree of fracturing, likely the result of external forces. It is presumed that the kimberlite magma within this pipe experienced significant violent disturbances.

Table 1. Common zonal relationships of #50 phlogopite in this study.

Back-Scattered Electron Image	Cartoon Showing Zoning	Feature Description
	low/poor Cr rim — rind — high-Ti-Cr core — rind	High-Ti-Cr Core: anhedral(embayed texture), Cr_2O_3 = 0.2–1.6 wt.%, TiO_2 = 2.2–3.5 wt.%, $Mg^\#$ = 88.2 Low-Cr/Cr-Poor Rim: Cr_2O_3 < 0.2 wt.%, TiO_2 = 2.5–5.4 wt.%, $Mg^\#$ = 82.4 Rind I: Cr_2O_3 < 0.12 wt.%, TiO_2 < 1.7 wt.%, $Mg^\#$ = 88.4
	low/poor Cr rim — low-Ti-Cr core	Low-Ti-Cr Core: anhedral(embayed texture), Cr_2O_3 < 1.0 wt.%, TiO_2 < 1.3 wt.%, $Mg^\#$ = 90.6 Low-Cr/Cr-Poor Outer Rim: Cr_2O_3 < 0.2 wt.%, TiO_2 = 2.5–5.4 wt.%, $Mg^\#$ = 82.4
	low-Ti-Cr core — high-Ti-Cr inner rim — low/poor Cr outer rim	Low-Ti-Cr Core: anhedral(embayed texture), Cr_2O_3 < 1.0 wt.%, TiO_2 < 1.3 wt.%, $Mg^\#$ = 90.6 High-Ti-Cr Inner Rim: Cr_2O_3 = 0.2–1.6 wt.%, TiO_2 = 2.2–3.5 wt.%, $Mg^\#$ = 88.2 Low-Cr/Cr-Poor Outer Rim: Cr_2O_3 < 0.2 wt.%, TiO_2 = 2.5–5.4 wt.%, $Mg^\#$ = 82.4
	high-Ti-Cr core — low/poor Cr rim — rind	High-Ti-Cr Core: euhedral, Cr_2O_3 = 0.2–1.6 wt.%, TiO_2 = 2.2–3.5 wt.%; $Mg^\#$ = 88.2 Low-Cr/Cr-Poor Rim: Cr_2O_3 < 0.2 wt.%, TiO_2 = 2.5–5.4 wt.%, $Mg^\#$ = 82.4 Rind II: Cr_2O_3 > 0.2 wt.%, TiO_2 = 2.5–3.5 wt.%, $Mg^\#$ = 88.6

No. 50 pipe kimberlite   No. 110 pipe kimberlite
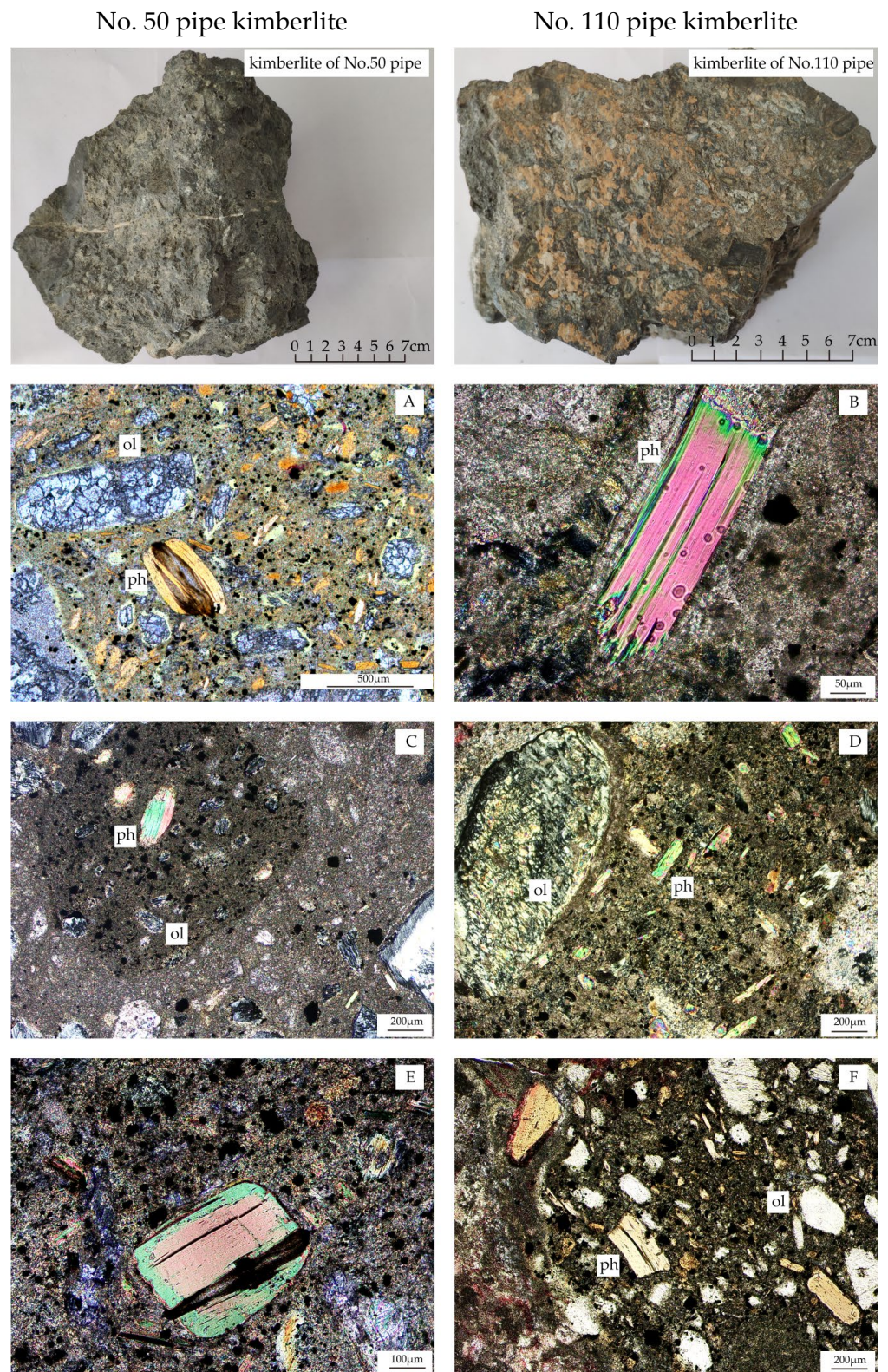
Figure 2. Representative images showing the different petrographic features of the No. 50 pipe kimberlite (**A**,**C**,**E**) and No. 110 pipe kimberlite (**B**,**D**,**F**). A and F are plane-polarized transmitted light photomicrographs. (**B**–**E**) are cross-polarized transmitted light photomicrographs. Ol—olivine, Phl—phlogopite.
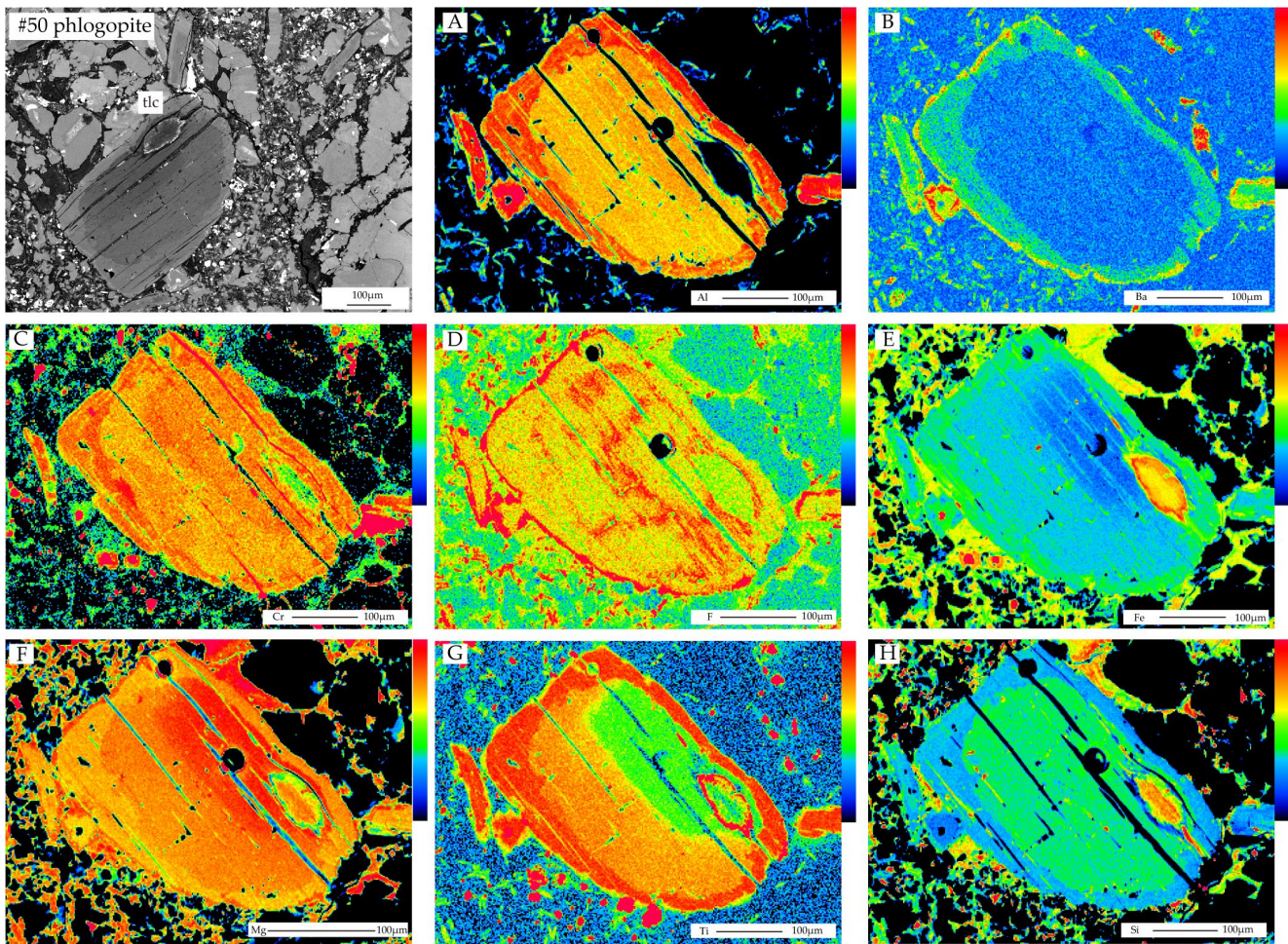
Figure 3. Back-scattered electron (BSE) image and X-ray elemental maps of a typical #50 phlogopite crystal from the No. 50 pipe kimberlite (Tlc-Talc). The colored scales on the right of each panel indicate the relative concentration of each element, i.e., "cool" colors (blue, black) = low concentrations, and "warm" colors (red, orange) = high concentrations. (**A**) Represents the Al concentration of the #50 phlogopite crystal, (**B**) represents the Ba concentration, (**C**) represents the Cr concentration, (**D**) represents the F concentration, (**E**) represents the Fe concentration, (**F**) represents the Mg concentration, (**G**) represents the Ti concentration, and (**H**) represents the Si concentration.
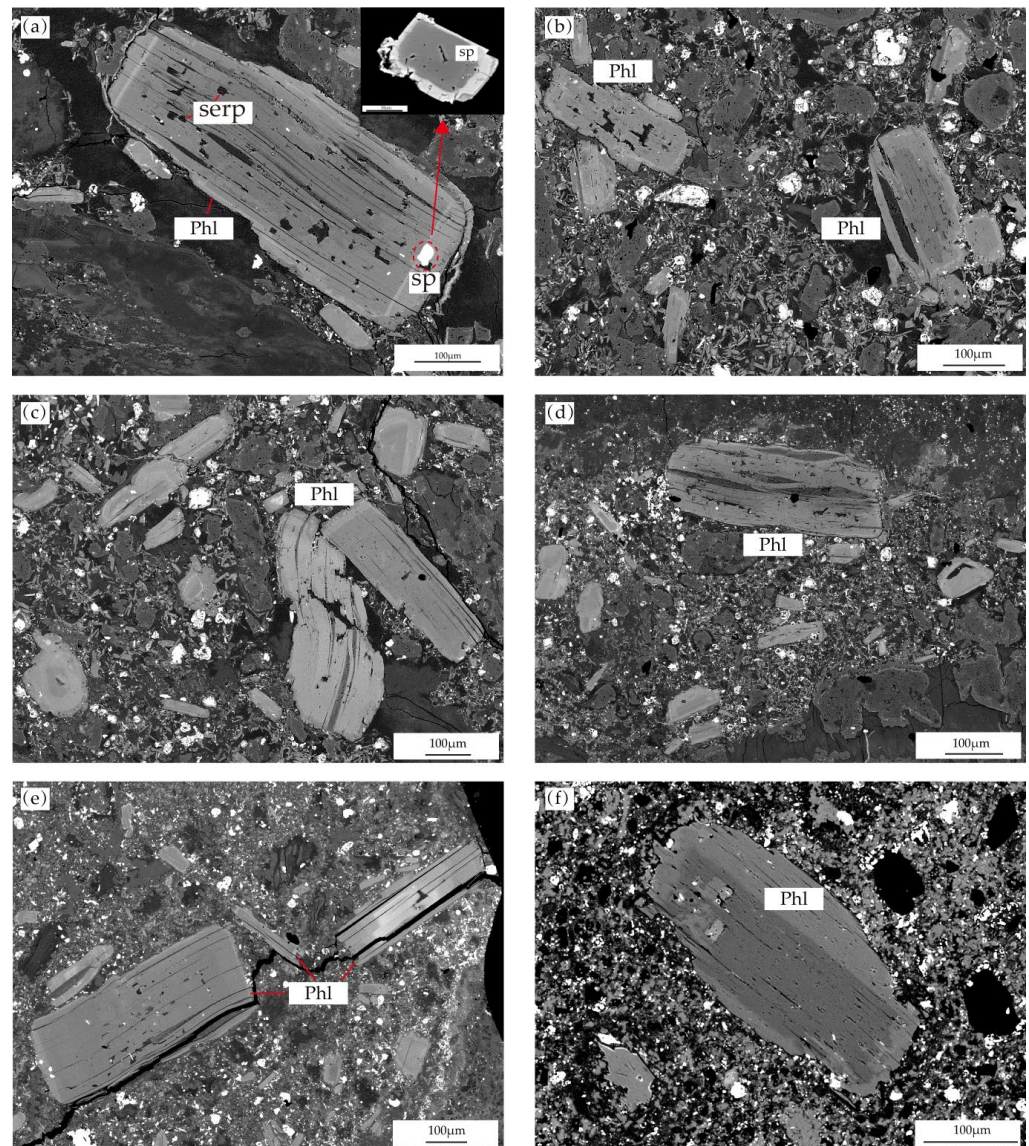
Figure 4. Back-scattered electron images showing examples of #50 phlogopite in the No. 50 pipe kimberlite. Sp—Spinel, Serp—serpentine, Phl—phlogopite. (**a**) The core of the phlogopite crystals is often filled with serpentine, and the rim with spinel inclusions. (**b**) The darker low-Ti-Cr core with embayed texture. (**c**,**d**) Deformed, twisted phlogopite crystals. (**e**) The more euhedral high-Ti-Cr core. (**f**) The darker low-T-Cr core is surrounded by the lighter high-Ti-Cr inner rim.
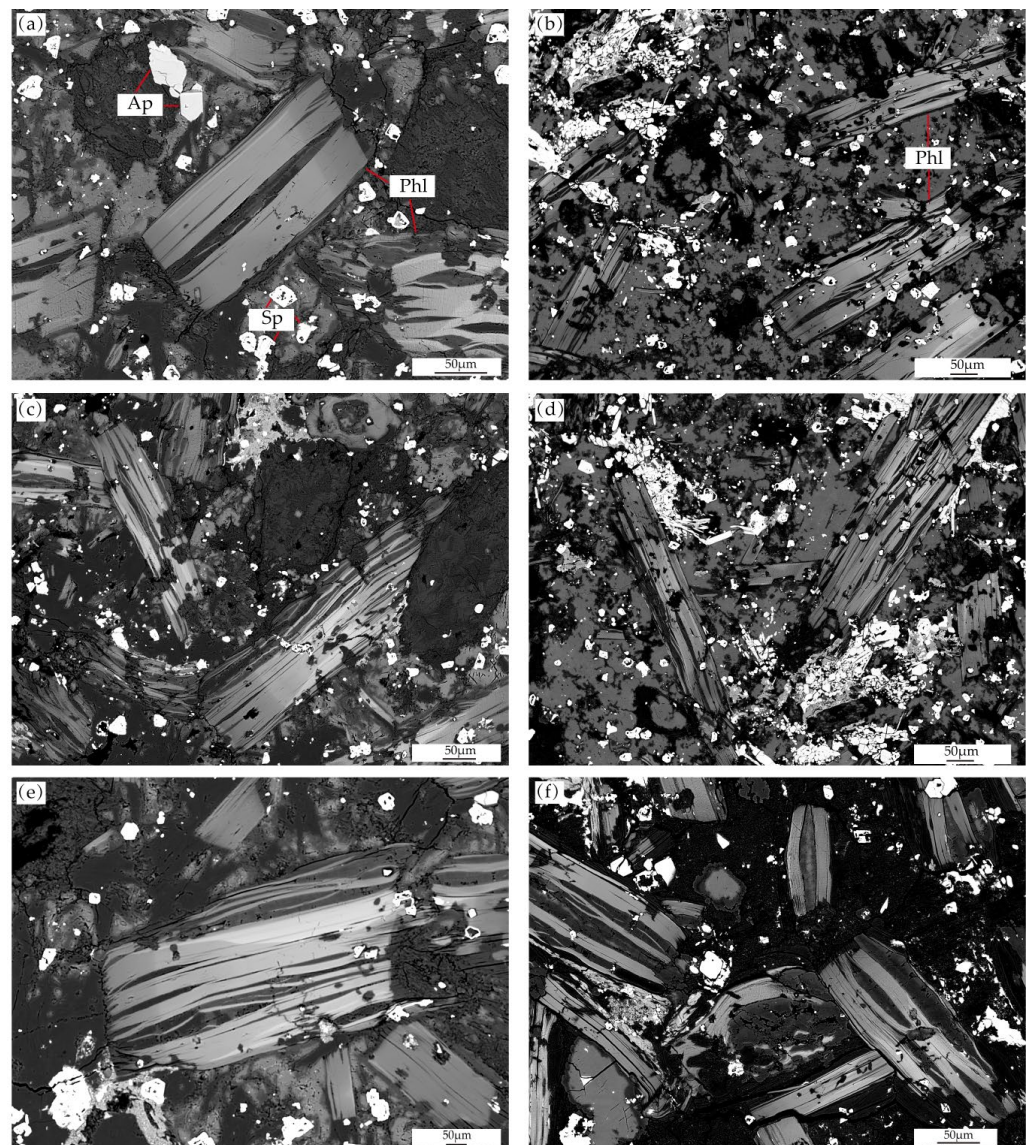
Figure 5. Back-scattered electron images showing examples of #110 phlogopite in the No. 110 pipe kimberlite. Phl—phlogopite, Sp—spinel, Ap—apatite. (**a**) more euhedral phlogopite crystal. (**b**–**f**) The phlogopite crystals are generally deformed and distorted, and there are often spinel inclusions in the crystals, a large amount of spinel and apatite in the matrix, and serpentine is filled along the cleavage of phlogopite.

5. Results

In the core of phlogopite #50, two types of components exist, one with low concentrations of Ti and Cr and another with high concentrations of Ti and Cr. Both types often exhibit outer rims with low levels of Cr. The high Ti-Cr cores typically exhibit a higher degree of euhedral morphology and rarely display the resorption structures that are observed in the low Ti-Cr cores. The composition of the high-Ti-Cr cores is characterized by higher abundances of Cr, Al, and Ba and lower levels of Si and Mg$^{\#}$, and the Mg$^{\#}$ values are more stable. Furthermore, apart from a few instances in which high Ti-Cr zones form the core, most of these zones surround the low Ti-Cr core as a mantle (inner rims). The compositions of the low-Cr/Cr-poor rims exhibit similarities to those of the groundmass phlogopite, with frequent occurrences of spinel or apatite inclusions within this zone. Compared to the cores and inner rims, the low-Cr/Cr-poor outer rims exhibit greater enrichment in Al and Ba and depletion in Cr, Ni, and Mg. This trend is characterized by a continuous decrease in Mg$^{\#}$ and a gradual increase in the Al and Ba contents from the interior outward

(from low-Ti-Cr cores to high-Ti-Cr inner rims to low-Cr/Cr-poor outer rims) (Table 2). X-ray images reveal the presence of rare and narrow rinds in the outermost layer of the phlogopite macrocrystals enriched in Mg (Figure 3F).

Table 2. Major element composition (wt.%) of #50 phlogopite in the studied samples.

Sample	F	Na$_2$O	SiO$_2$	Al$_2$O$_3$	MgO	Cl	K$_2$O	CaO	NiO	FeO	MnO	Cr$_2$O$_3$	TiO$_2$	BaO	Total	Mg$^\#$
							Low-Ti-Cr Cores									
#50-3	0.526	0.127	41.800	11.556	24.161	0.023	10.365	0.086	0.019	5.423	0.072	0.372	0.973	0.000	95.277	88.8
#50-13	0.777	0.041	39.882	13.037	25.338	0.006	9.879	0.037	0.078	4.593	0.037	0.038	0.874	1.501	95.790	90.8
#50-14	0.261	0.054	41.832	12.153	24.689	0.027	10.150	0.070	0.212	4.584	0.018	0.714	0.885	0.095	95.628	90.6
#50-16	0.231	0.157	42.184	11.856	25.128	0.029	10.431	0.033	0.260	3.841	0.008	0.767	0.952	0.054	95.827	92.1
#50-17	0.457	0.130	42.362	11.889	25.046	0.000	10.460	0.070	0.225	3.613	0.045	0.805	1.035	0.061	96.006	92.5
#50-22	0.901	0.043	38.864	12.283	24.991	0.000	10.016	0.000	0.000	4.858	0.089	0.034	1.159	1.324	94.183	90.2
#50-36	0.359	0.083	41.072	11.932	24.145	0.041	10.311	0.031	0.094	4.823	0.037	0.590	1.151	0.115	94.624	89.9
#50-41	0.451	0.036	41.589	12.204	24.305	0.046	10.131	0.016	0.141	5.358	0.043	0.352	1.078	0.122	95.672	89.0
#50-42	0.476	0.111	41.263	10.472	24.564	0.000	10.422	0.077	0.218	5.066	0.000	0.721	1.301	0.047	94.538	89.6
#50-47	0.395	0.070	41.478	11.747	24.819	0.028	10.692	0.087	0.134	4.445	0.033	0.582	1.106	0.007	95.451	90.9
#50-56	0.631	0.154	39.639	11.436	24.376	0.007	9.713	0.117	0.011	5.422	0.056	0.038	1.164	1.042	93.538	88.9
#50-70	0.450	0.043	41.312	11.969	24.448	0.017	10.379	0.021	0.241	4.303	0.000	0.806	1.180	0.081	95.057	91.0
#50-71	0.617	0.074	41.000	11.674	24.167	0.034	10.579	0.000	0.164	4.172	0.041	0.770	1.035	0.054	94.113	91.2
#50-74	0.808	0.007	40.719	11.837	24.216	0.023	9.846	0.011	0.130	5.491	0.033	0.266	1.197	0.000	94.239	88.7
#50-76	0.375	0.054	41.384	11.589	24.445	0.057	10.226	0.000	0.177	4.693	0.029	0.600	0.917	0.101	94.476	90.3
#50-78	0.198	0.063	40.505	12.894	24.200	0.096	10.830	0.000	0.162	3.679	0.058	0.983	0.632	0.176	94.371	92.1
#50-88	0.429	0.034	41.910	11.769	24.517	0.004	10.561	0.000	0.135	5.277	0.000	0.260	0.956	0.020	95.690	89.2
#50-118	0.289	0.043	41.563	11.780	24.353	0.037	10.534	0.000	0.203	4.510	0.041	0.585	1.127	0.102	95.037	90.6
#50-121	0.271	0.085	41.388	12.693	24.953	0.064	10.384	0.056	0.188	3.366	0.000	0.843	0.451	0.062	94.676	93.0
							High-Ti-Cr Cores/Inner Rims									
#50-1	0.242	0.035	38.921	14.068	22.693	0.000	10.482	0.000	0.021	4.964	0.039	1.105	3.460	0.306	96.234	89.1
#50-5	0.096	0.119	41.360	12.624	22.760	0.026	10.439	0.013	0.172	4.799	0.000	1.400	2.411	0.020	96.193	89.4
#50-8	0.253	0.101	38.825	14.292	23.057	0.000	10.317	0.026	0.144	4.442	0.008	1.186	2.944	0.454	95.942	90.2
#50-15	0.245	0.041	38.634	14.753	23.121	0.000	10.078	0.019	0.028	4.787	0.058	1.268	2.946	0.345	96.220	89.6
#50-24	0.145	0.050	37.471	15.036	22.706	0.000	10.059	0.008	0.072	4.903	0.056	0.868	3.087	0.723	95.123	89.2
#50-27	0.205	0.048	37.825	13.938	22.918	0.000	10.481	0.000	0.081	4.345	0.016	1.189	3.023	0.624	94.607	90.4
#50-28	0.206	0.087	39.264	13.126	22.871	0.000	10.597	0.021	0.028	5.484	0.041	0.846	2.593	0.310	95.387	88.1
#50-35	0.251	0.034	38.325	14.263	22.982	0.006	10.206	0.008	0.105	4.232	0.070	1.246	3.222	0.438	95.281	90.6
#50-37	0.158	0.193	40.611	12.675	23.004	0.032	10.238	0.039	0.086	5.016	0.029	0.769	2.626	0.229	95.631	89.1
#50-43	0.308	0.041	37.940	14.291	22.297	0.001	10.295	0.032	0.075	4.307	0.056	1.256	3.139	0.558	94.466	90.2
#50-46	0.258	0.047	38.437	13.774	23.202	0.000	10.46	0.010	0.135	4.076	0.000	0.901	2.921	0.330	94.442	91.0
#50-48	0.194	0.016	37.860	14.963	22.978	0.000	9.812	0.018	0.075	4.791	0.100	1.015	3.301	0.639	95.680	89.5
#50-49	0.175	0.050	37.880	14.809	22.542	0.000	10.419	0.031	0.113	4.355	0.046	1.177	2.927	0.612	95.062	90.2
#50-54	0.104	0.077	37.561	14.986	22.459	0.005	9.814	0.096	0.077	4.833	0.037	0.975	2.933	0.611	94.523	89.2
#50-57	0.389	0.079	40.907	12.161	23.363	0.015	9.952	0.019	0.180	4.814	0.042	0.767	2.112	0.061	94.694	89.6
#50-58	0.280	0.050	37.734	14.024	22.567	0.007	9.716	0.016	0.099	4.606	0.012	1.254	3.041	0.429	93.715	89.7
#50-61	0.139	0.020	39.555	12.808	21.98	0.024	10.362	0.034	0.183	4.594	0.021	1.658	2.735	0.08	94.129	89.5
#50-68	0.096	0.212	38.627	13.836	22.304	0.004	10.111	0.000	0.139	5.294	0.029	1.456	2.173	0.295	94.535	88.2
#50-69	0.278	0.044	38.036	13.505	22.599	0.000	9.678	0.000	0.074	5.260	0.064	1.256	2.955	0.420	94.052	88.5
#50-72	0.179	0.016	37.783	14.324	22.940	0.000	10.257	0.000	0.124	4.577	0.046	1.237	2.900	0.585	94.893	89.9
#50-77	0.161	0.039	37.701	14.321	22.908	0.007	10.422	0.023	0.066	4.572	0.099	1.176	3.376	0.337	95.138	89.9
#50-79	0.221	0.007	38.131	14.463	22.599	0.009	10.242	0.000	0.051	4.417	0.043	1.148	3.166	0.628	95.030	90.1
#50-81	0.276	0.027	37.940	13.970	22.686	0.000	10.397	0.006	0.058	4.859	0.037	1.131	3.201	0.479	94.951	89.3
#50-85	0.265	0.080	39.156	14.132	22.704	0.002	10.478	0.000	0.115	5.074	0.006	1.120	3.102	0.332	96.454	88.9
#50-90	0.295	0.094	40.354	12.397	22.845	0.010	10.463	0.019	0.142	4.702	0.033	0.808	2.998	0.163	95.197	89.6
#50-91	0.277	0.057	38.776	13.549	23.285	0.026	10.229	0.000	0.119	4.630	0.043	0.814	2.835	0.394	94.911	90.0
#50-99	0.170	0.032	40.553	13.349	22.737	0.032	10.739	0.000	0.186	4.546	0.000	1.745	2.305	0.014	96.329	89.9
#50-102	0.260	0.044	38.942	14.505	23.232	0.000	10.278	0.000	0.013	4.803	0.094	1.201	3.252	0.435	96.95	89.6
#50-112	0.127	0.115	40.144	12.575	22.469	0.015	10.500	0.000	0.199	4.463	0.033	1.378	2.645	0.000	94.607	90.0
#50-117	0.216	0.092	37.801	14.136	22.340	0.000	10.387	0.000	0.104	4.355	0.000	1.300	3.035	0.470	94.145	90.1
#50-119	0.284	0.032	38.946	12.979	22.436	0.026	10.385	0.010	0.248	4.617	0.047	1.640	2.592	0.088	94.204	89.6
#50-120	0.313	0.066	39.395	13.883	23.185	0.000	10.12	0.021	0.066	4.792	0.039	1.066	3.196	0.292	96.302	89.6
#50-122	0.277	0.099	39.174	13.500	22.912	0.000	10.316	0.094	0.103	5.154	0.074	0.833	2.863	0.578	95.860	88.8
#50-124	0.255	0.126	38.39	14.376	22.553	0.000	10.197	0.044	0.061	4.512	0.000	0.902	3.139	0.483	94.931	89.9
#50-75	0.231	0.002	36.792	15.229	22.418	0.000	10.116	0.024	0.128	5.131	0.052	0.603	3.255	1.271	95.155	88.6
#50-59	0.130	0.045	37.913	14.118	22.711	0.022	10.230	0.024	0.073	4.888	0.013	0.608	3.224	0.550	94.489	89.2
#50-31	0.272	0.075	38.997	13.38	22.714	0.000	10.231	0.003	0.053	5.823	0.041	0.660	2.354	0.296	94.784	87.4
#50-86	0.241	0.090	37.992	13.901	22.394	0.000	10.471	0.008	0.068	5.849	0.052	0.592	2.771	0.365	94.693	87.2

Table 2. *Cont.*

Sample	F	Na$_2$O	SiO$_2$	Al$_2$O$_3$	MgO	Cl	K$_2$O	CaO	NiO	FeO	MnO	Cr$_2$O$_3$	TiO$_2$	BaO	Total	Mg#
#50-2	0.293	0.090	36.790	15.268	22.014	0.018	10.006	0.105	0.079	5.619	0.052	0.214	3.264	1.204	94.889	87.5
#50-4	0.086	0.012	36.847	15.396	22.416	0.000	10.043	0.023	0.026	5.588	0.017	0.259	3.419	1.285	95.381	87.7
#50-9	0.235	0.044	37.517	15.358	22.612	0.000	10.104	0.044	0.059	5.234	0.039	0.343	3.645	1.272	96.407	88.5
#50-12	0.231	0.035	37.419	15.501	22.138	0.012	10.14	0.047	0.096	5.158	0.085	0.334	3.348	1.367	95.811	88.4
#50-20	0.325	0.052	39.039	13.695	22.654	0.018	10.272	0.000	0.000	4.242	0.045	0.255	3.290	0.427	94.173	90.5
#50-25	0.236	0.039	36.691	15.447	22.574	0.000	10.205	0.026	0.000	5.261	0.035	0.297	3.443	1.356	95.511	88.4
#50-26	0.196	0.037	36.665	15.754	22.457	0.006	10.017	0.06	0.085	5.454	0.099	0.348	3.485	1.167	95.746	88.0
#50-33	0.226	0.055	36.500	15.709	22.509	0.000	10.253	0.019	0.028	5.081	0.079	0.354	3.408	1.298	95.424	88.8
#50-34	0.227	0.035	37.037	14.801	22.425	0.016	10.069	0.045	0.086	6.164	0.095	0.224	3.915	1.45	96.489	86.6
#50-38	0.202	0.062	36.792	15.9	22.788	0.006	10.141	0.014	0.021	5.197	0.004	0.282	3.476	1.463	96.262	88.7
#50-44	0.092	0.016	36.562	15.506	22.159	0.014	10.182	0.058	0.049	5.032	0.039	0.318	3.562	1.497	95.044	88.7
#50-50	0.190	0.032	36.67	15.357	22.215	0.000	9.928	0.000	0.066	5.199	0.091	0.416	3.313	1.255	94.652	88.4
#50-51	0.298	0.041	38.809	13.293	23.208	0.022	10.486	0.024	0.060	4.648	0.046	0.383	2.792	0.344	94.324	89.9
#50-52	0.344	0.059	36.371	15.658	22.187	0.002	9.722	0.011	0.045	5.211	0.056	0.384	3.203	1.033	94.141	88.4
#50-60	0.154	0.057	36.563	15.054	22.061	0.010	9.930	0.067	0.114	5.38	0.038	0.296	3.364	1.378	94.399	88.0
#50-64	0.211	0.116	38.727	13.916	22.483	0.002	10.243	0.000	0.049	5.335	0.031	0.402	2.984	0.409	94.819	88.3
#50-65	0.158	0.062	36.501	15.347	22.167	0.000	10.101	0.000	0.052	5.249	0.046	0.330	3.165	1.238	94.349	88.3
#50-73	0.108	0.042	36.049	15.101	22.333	0.007	10.029	0.002	0.132	5.502	0.105	0.336	3.132	1.266	94.097	87.9
#50-80	0.207	0.163	39.886	12.807	22.11	0.036	10.332	0.000	0.134	5.495	0.014	0.494	3.424	0.223	95.230	87.8
#50-82	0.136	0.048	36.558	14.449	22.434	0.002	9.892	0.039	0.094	5.649	0.050	0.393	3.372	1.085	94.144	87.6
#50-93	0.192	0.032	37.173	15.292	22.243	0.007	10.098	0.013	0.006	5.786	0.049	0.219	3.411	1.225	95.663	87.3
#50-103	0.104	0.147	38.639	14.493	21.738	0.000	10.296	0.000	0.021	6.731	0.092	0.377	2.927	0.435	95.956	85.2
#50-104	0.212	0.019	36.961	15.355	22.954	0.009	10.039	0.000	0.108	5.461	0.057	0.242	3.444	1.236	96.006	88.2
#50-105	0.187	0.042	37.140	15.333	22.615	0.000	9.971	0.026	0.108	5.452	0.074	0.301	3.622	1.244	96.036	88.1
#50-110	0.096	0.042	36.977	15.434	22.388	0.000	10.251	0.000	0.036	5.649	0.068	0.217	3.417	1.408	95.943	87.6
#50-111	0.132	0.085	36.481	14.991	21.522	0.007	9.969	0.006	0.144	5.688	0.071	0.203	3.589	1.151	93.981	87.1
#50-113	0.148	0.028	36.312	15.293	22.158	0.000	10.226	0.002	0.042	5.099	0.076	0.317	3.468	1.249	94.356	88.6
#50-114	0.248	0.210	38.493	14.496	21.986	0.000	10.116	0.013	0.040	5.945	0.020	0.221	2.691	0.483	94.858	86.8
#50-115	0.237	0.037	36.371	15.23	22.333	0.000	10.202	0.042	0.081	5.349	0.062	0.332	3.244	1.392	94.812	88.2
#50-116	0.302	0.110	39.535	12.236	21.827	0.002	10.140	0.024	0.076	7.298	0.117	0.486	3.149	0.407	95.582	84.2
#50-125	0.277	0.095	36.736	15.617	22.269	0.000	9.761	0.065	0.049	5.307	0.070	0.328	2.997	1.284	94.738	88.2
#50-7	0.236	0.250	38.21	14.464	18.881	0.017	10.011	0.016	0.036	9.473	0.118	0.659	2.684	0.276	95.228	78.0
#50-97	0.138	0.074	36.199	17.45	19.233	0.004	9.888	0.000	0.089	8.852	0.097	0.224	2.661	0.891	95.741	79.5
#50-18	0.281	0.056	39.128	12.375	22.086	0.000	10.019	0.040	0.117	7.565	0.048	0.365	3.533	0.371	95.866	83.9
#50-100	0.256	0.264	37.926	14.443	20.394	0.000	10.356	0.000	0.051	8.168	0.080	0.476	3.145	0.338	95.789	81.7
#50-101	0.074	0.125	38.133	14.145	20.346	0.013	10.189	0.000	0.070	7.956	0.041	0.409	3.411	0.264	95.142	82.0
Low-Cr/Cr-Poor Outer Rims																
#50-19	0.166	0.019	37.756	13.054	22.438	0.009	10.057	0.006	0.055	7.457	0.041	0.197	3.257	0.438	94.878	84.3
#50-87	0.164	0.030	36.634	15.766	22.422	0.000	10.103	0.039	0.057	5.211	0.047	0.196	3.546	1.542	95.688	88.5
#50-6	0.279	0.051	37.108	15.115	22.433	0.000	9.894	0.000	0.051	5.704	0.054	0.140	3.519	1.414	95.645	87.5
#50-10	0.830	0.081	40.667	10.578	25.349	0.000	9.250	0.115	0.057	7.398	0.029	0.009	0.654	0.502	95.170	85.9
#50-11	1.092	0.074	37.828	14.457	15.961	0.064	10.091	0.000	0.000	11.838	0.039	0.007	5.431	0.689	97.097	70.6
#50-21	0.224	0.042	36.976	14.786	22.631	0.000	10.150	0.016	0.057	5.915	0.052	0.004	2.700	1.418	94.877	87.2
#50-23	0.240	0.089	38.110	14.088	18.308	0.012	10.025	0.016	0.036	11.445	0.106	0.027	2.524	0.381	95.303	74.0
#50-29	0.254	0.059	38.029	13.014	19.828	0.011	10.328	0.000	0.041	8.464	0.094	0.000	4.713	0.442	95.168	80.7
#50-30	0.255	0.028	38.679	13.621	20.726	0.012	9.807	0.013	0.000	8.502	0.093	0.009	4.204	0.349	96.188	81.3
#50-32	0.300	0.019	39.447	11.834	21.175	0.000	10.105	0.008	0.034	8.620	0.075	0.029	3.611	0.101	95.232	81.4
#50-39	0.203	0.174	37.362	13.444	19.205	0.010	9.897	0.029	0.101	10.243	0.094	0.000	4.048	0.573	95.296	77.0
#50-40	0.246	0.050	36.788	15.114	21.996	0.000	9.818	0.000	0.049	5.423	0.035	0.110	3.395	1.504	94.424	87.8
#50-45	0.263	0.142	37.727	14.129	20.482	0.000	9.860	0.000	0.000	7.360	0.121	0.062	3.788	0.59	94.413	83.2
#50-53	0.112	0.081	35.589	17.416	17.890	0.018	9.791	0.051	0.037	10.755	0.098	0.035	2.345	0.672	94.839	74.8
#50-55	0.218	0.117	36.751	14.769	21.804	0.000	9.527	0.115	0.009	5.958	0.121	0.085	3.658	1.338	94.378	86.7
#50-62	0.193	0.058	36.521	14.729	21.782	0.027	9.748	0.047	0.089	5.823	0.058	0.036	3.106	1.428	93.558	87.0
#50-63	0.226	0.197	36.689	16.109	19.393	0.000	10.091	0.003	0.045	8.006	0.025	0.132	2.601	0.493	93.915	81.2
#50-66	0.183	0.126	38.620	12.223	22.296	0.000	10.318	0.047	0.066	6.963	0.045	0.079	2.923	0.576	94.388	85.1
#50-67	0.133	0.072	37.201	12.986	18.633	0.022	10.002	0.058	0.015	10.029	0.136	0.033	4.464	0.504	94.227	76.8
#50-83	0.217	0.235	38.399	13.332	20.645	0.004	10.218	0.000	0.000	8.548	0.066	0.127	3.155	0.337	95.191	81.1
#50-84	0.222	0.228	38.936	13.271	20.572	0.004	10.133	0.027	0.008	8.723	0.070	0.147	3.165	0.357	95.769	80.8
#50-89	0.288	0.000	38.239	13.755	22.741	0.007	10.104	0.000	0.000	6.614	0.010	0.173	3.204	0.886	95.898	86.0
#50-92	0.377	0.074	37.228	14.914	22.367	0.000	9.817	0.006	0.036	6.034	0.062	0.000	3.460	1.353	95.569	86.9
#50-94	0.179	0.072	36.900	15.370	22.278	0.007	9.886	0.010	0.006	5.849	0.008	0.084	3.690	1.317	95.579	87.2
#50-95	0.157	0.155	37.133	13.892	20.080	0.012	9.902	0.000	0.000	9.666	0.083	0.040	3.361	0.593	95.005	78.7
#50-96	0.322	0.194	35.327	15.541	16.218	0.018	9.395	0.000	0.008	13.862	0.141	0.020	3.468	1.001	95.375	67.6
#50-98	0.279	0.014	36.395	15.192	22.321	0.000	9.500	0.000	0.089	6.516	0.070	0.054	3.144	1.435	94.892	85.9
#50-106	0.216	0.079	38.722	13.368	22.400	0.005	10.312	0.016	0.023	6.730	0.025	0.029	3.697	0.483	96.013	85.6

Table 2. *Cont.*

Sample	F	Na$_2$O	SiO$_2$	Al$_2$O$_3$	MgO	Cl	K$_2$O	CaO	NiO	FeO	MnO	Cr$_2$O$_3$	TiO$_2$	BaO	Total	Mg$^\#$
#50-107	0.133	0.090	37.117	15.076	20.077	0.011	10.301	0.000	0.000	8.712	0.035	0.022	3.160	0.759	95.435	80.4
#50-108	0.240	0.153	38.297	13.684	21.577	0.006	10.176	0.019	0.072	7.691	0.082	0.027	3.515	0.468	95.905	83.3
#50-109	0.357	0.049	39.266	11.884	23.156	0.000	10.294	0.024	0.000	7.139	0.066	0.016	2.694	0.293	95.088	85.3
#50-123	0.196	0.042	36.337	14.712	22.056	0.010	10.044	0.065	0.036	6.184	0.053	0.068	3.605	1.179	94.502	86.4
Rind I (low-Ti-Cr)																
#50-1	0.784	0.032	40.295	9.773	24.606	0.006	10.158	0.091	0.073	7.018	0.066	0.011	1.677	0.507	94.778	86.2
#50-2	0.949	0.054	40.606	11.962	24.635	0.000	10.084	0.139	0.044	4.691	0.033	0.025	0.982	1.125	94.971	90.4
#50-4	0.886	0.057	40.185	12.465	25.626	0.000	10.079	0.099	0.051	4.951	0.078	0.049	0.931	0.792	95.875	90.2
#50-5	0.946	0.066	39.887	12.056	25.518	0.002	10.537	0.024	0.013	4.650	0.015	0.064	0.813	1.118	95.312	90.7
#50-6	0.913	0.048	39.722	12.060	25.305	0.000	10.474	0.038	0.085	5.028	0.057	0.000	0.882	1.035	95.281	90.0
#50-7	0.848	0.040	40.522	12.618	24.023	0.000	10.274	0.047	0.066	4.940	0.057	0.008	1.220	1.374	95.682	89.7
#50-8	0.675	0.031	39.477	11.230	25.938	0.013	10.088	0.111	0.035	6.562	0.032	0.032	1.269	0.859	96.092	87.6
#50-9	0.878	0.054	41.436	11.523	25.517	0.001	10.119	0.041	0.013	5.768	0.052	0.004	0.882	0.621	96.566	88.8
#50-10	1.068	0.010	41.629	10.573	25.033	0.003	10.319	0.039	0.126	5.903	0.084	0.015	0.836	0.555	95.744	88.3
#50-11	0.933	0.028	41.456	10.821	23.894	0.012	10.136	0.072	0.058	5.649	0.028	0.045	0.964	0.506	94.204	88.3
#50-12	1.062	0.046	40.451	11.462	23.428	0.006	9.661	0.139	0.070	6.008	0.080	0.077	1.564	0.985	94.625	87.4
#50-13	0.844	0.046	40.396	11.593	25.173	0.000	10.147	0.189	0.036	5.586	0.041	0.066	0.901	0.728	95.432	88.9
#50-14	1.002	0.028	40.940	10.776	24.149	0.005	10.230	0.054	0.028	5.707	0.055	0.036	1.025	0.639	94.255	88.3
#50-15	0.849	0.033	40.310	10.343	24.426	0.000	9.298	0.093	0.100	7.361	0.052	0.067	1.105	0.624	94.355	85.6
#50-18	0.997	0.034	40.860	10.377	24.350	0.000	10.099	0.161	0.065	5.911	0.045	0.089	1.079	0.675	94.364	88.0
#50-20	0.921	0.030	40.949	9.743	23.807	0.008	10.020	0.205	0.079	7.143	0.071	0.037	1.049	0.457	94.220	85.6
#50-24	0.951	0.036	41.331	11.233	24.849	0.000	9.524	0.142	0.063	6.086	0.037	0.053	0.797	0.779	95.506	87.9
#50-29	1.188	0.025	40.708	11.486	24.486	0.000	10.429	0.044	0.054	5.562	0.044	0.000	1.640	0.892	96.060	88.7
#50-30	1.401	0.024	41.849	9.936	23.243	0.000	10.370	0.820	0.031	5.882	0.110	0.108	1.284	0.445	94.920	87.6
#50-31	1.331	0.014	41.861	11.107	24.645	0.002	10.309	0.054	0.032	4.663	0.043	0.173	1.406	1.113	96.192	90.4
#50-36	0.892	0.070	39.421	12.885	25.606	0.003	9.969	0.238	0.084	4.659	0.060	0.041	0.948	1.741	96.242	90.8
#50-37	1.139	0.022	40.798	12.335	24.981	0.006	10.280	0.102	0.029	4.672	0.071	0.004	1.113	1.529	96.601	90.5
#50-38	1.012	0.040	40.280	12.368	24.540	0.001	10.060	0.096	0.081	4.651	0.037	0.000	1.049	1.803	95.626	90.4
#50-27	0.355	0.057	37.656	14.390	22.117	0.009	10.370	0.036	0.021	5.691	0.015	0.027	2.983	1.219	94.793	87.4
#50-28	0.446	0.136	39.567	11.921	22.253	0.001	10.395	0.048	0.048	7.012	0.035	0.102	2.726	0.535	95.052	85.0
#50-40	0.287	0.073	37.050	15.001	22.392	0.009	10.243	0.131	0.057	5.528	0.048	0.117	3.334	1.171	95.318	87.8
#50-32	1.088	0.046	40.315	10.943	24.097	0.000	10.363	0.030	10.363	6.301	0.072	0.012	1.690	0.886	95.423	87.2
Rind II (high-Ti-Cr)																
#50-17	0.426	0.101	40.133	12.201	22.078	0.015	10.395	0.189	0.049	5.051	0.036	0.938	2.579	0.254	94.279	88.6
#50-21	0.399	0.049	39.245	13.493	22.614	0.007	10.745	0.034	0.049	4.626	0.011	0.851	2.958	0.456	95.365	89.7
#50-22	0.400	0.055	39.222	13.824	22.332	0.000	10.503	0.063	0.065	4.677	0.010	0.927	3.068	0.528	95.505	89.5
#50-39	0.315	0.095	38.958	13.853	22.781	0.000	10.473	0.092	0.087	4.515	0.022	1.182	2.919	0.432	95.593	90.0
#50-25	0.378	0.076	37.018	14.569	21.765	0.001	9.982	0.094	0.040	5.451	0.058	0.211	3.451	1.413	94.385	87.7
#50-19	0.471	0.046	37.520	14.876	22.135	0.000	10.060	0.067	0.030	5.663	0.060	0.238	3.379	1.291	95.648	87.5
#50-35	0.277	0.054	37.293	15.033	22.076	0.002	10.516	0.010	0.033	5.295	0.067	0.371	3.386	1.221	95.516	88.2
#50-33	0.377	0.053	37.690	14.666	21.871	0.009	10.379	0.000	0.068	5.329	0.026	0.206	3.054	1.185	94.752	88.0
#50-34	0.333	0.055	37.865	15.016	21.555	0.003	10.370	0.045	0.041	5.253	0.045	0.240	3.134	1.485	95.298	88.0
#50-16	0.616	0.074	42.132	11.718	23.454	0.055	10.440	0.141	0.130	5.145	0.037	0.327	1.141	0.008	95.184	89.1

5.1. Low-Ti-Cr Core Composition of #50 Phlogopite

The composition of the low-Ti-Cr cores is relatively stable, except for the contents of Mg and Ni. The levels of other elements were found to be very low. The low-Ti-Cr cores exhibit a pronounced similarity to phlogopite from metasomatized peridotite xenoliths and often exhibit resorption (embayed texture) and deformation structures. The major elements are Cr$_2$O$_3$ < 1.0 wt.%, TiO$_2$ < 1.3 wt.%; Al$_2$O$_3$ = 10.5–13.0 wt.%; and average Mg$^\#$ = 90.6. The trace elements are Ba = 187.4–1383 ppm, Nb = 5.2–8.54 ppm, Sr = 3.2–8.7 ppm, and V = 80.1–129.8 ppm (Table S1).

5.2. High-Ti-Cr Core/Inner Rim Composition of #50 Phlogopite

The composition of the cores and inner rims with high Ti-Cr contents has a wide range, very similar to that of phlogopite from mantle xenoliths, including polymictic breccia [59]. In comparison to the outer rims and groundmass with low Cr and high Ti contents, the high-Ti-Cr zone (cores and inner rims) exhibits higher concentrations of Mg, Cr, and Ni (Figure 6A,C,E). The major elements of the high-Ti-Cr inner rims/cores are Cr$_2$O$_3$ = 0.2–1.6 wt.%, TiO$_2$ = 2.2–3.5 wt.%, and Al$_2$O$_3$ = 12.4–15.7 wt.%, with an average

Mg$^{\#}$ = 88.2. The trace element composition includes Ba = 640–5602 ppm, Nb = 6.8–19.6 ppm, Sr = 9.1–95.6 ppm, and V = 60.1–185.3 ppm.

5.3. Low-Cr/Cr-Poor Outer Rim Composition of #50 Phlogopite

Low-Cr outer rims were defined as those containing 0.1–0.2 wt.% Cr$_2$O$_3$, while Cr-poor outer rims were defined as those containing less than 0.1 wt.% Cr$_2$O$_3$. As these regions often occur as the outer layers of phlogopite crystals, they are collectively referred to as low-Cr/Cr-poor outer rims for statistical convenience. The major components of the low-Cr/Cr-poor outer rims are Cr$_2$O$_3$ < 0.2 wt.%, TiO$_2$ = 2.5–5.4 wt.%, and Al$_2$O$_3$ = 13.1–16.1 wt.%, with an average Mg$^{\#}$ = 82.4. The trace elements are Ba = 2367–10,870 ppm, Nb = 19.4–41.6 ppm, Sr = 22.2–129.7 ppm, and V = 34.6–301.4 ppm.

5.4. Rind I (Low-Ti-Cr) and Rind II (High-Ti-Cr) Composition of #50 Phlogopite

The rinds display complex compositional distributions, and they are relatively uncommon. There are two composition trends in the rinds, namely, (1) low-Ti-Cr rinds, defined in this paper as rind I, and (2) high-Ti-Cr rinds, defined as rind II. The major elements of rind I are Cr$_2$O$_3$ < 0.12 wt.%, TiO$_2$ < 1.7 wt.%, and Al$_2$O$_3$ = 9.7–12.9 wt.%, with an average Mg$^{\#}$ = 88.4. The major elements of rind II are Cr$_2$O$_3$ > 0.2 wt.%, TiO$_2$ = 2.5–3.5 wt.%, and Al$_2$O$_3$ = 12.2–15.0 wt.%, with an average Mg$^{\#}$ = 88.6. The rind composition is characterized by a re-enrichment of Mg, with a slight decrease in Al content from the low-Cr/Cr-poor outer rims to the rinds. However, there is a gradual increase in the Al concentration from rind I (low Ti-Cr) to rind II (high Ti-Cr rinds). In addition, rind I has a high content of F (0.3–1.4 wt.%).

5.5. Composition of #110 Phlogopite

Although zonation is present in the #110 phlogopite, the compositions of these zones are highly concentrated and lack the distinct variation observed in the #50 phlogopite. For ease of statistical analysis, these grains have not been further subdivided but rather uniformly referred to as the #110 phlogopite.

The composition of the #110 phlogopite features the enrichment of Mg and F (Table 3), which is also found in the Aries kimberlite, a hypabyssal macrocrystic phlogopite kimberlite (MPK) [23]. Mg and F enrichment are also observed in rind I (low-Ti-Cr rind) of the #50 phlogopite. In addition, the #110 phlogopite is significantly more enriched in Al and Ba. The #110 phlogopite major element composition is Cr$_2$O$_3$ < 0.1 wt.%, TiO$_2$ = 0.6–1.9 wt.%, and Al$_2$O$_3$ = 13.1–16.5 wt.%, with an average Mg$^{\#}$ = 90.1. The F content of the #110 phlogopite is very close to that of rind I, both of which exhibit very high levels (0.9–1.2 wt.%).

Table 3. Major element composition (wt.%) of #110 phlogopite in the studied samples.

Sample	F	Na$_2$O	SiO$_2$	Al$_2$O$_3$	MgO	Cl	K$_2$O	CaO	NiO	FeO	MnO	Cr$_2$O$_3$	TiO$_2$	BaO	Total	Mg$^{\#}$
#110-1	1.225	0.018	38.278	13.886	23.869	0.008	9.936	0.011	0.026	4.795	0.060	0.056	1.229	2.509	95.391	89.9
#110-2	1.083	0.109	35.982	15.778	23.237	0.007	9.115	0.015	0.042	4.569	0.091	0.057	1.488	5.188	96.315	90.1
#110-3	1.149	0.054	34.410	16.381	22.856	0.000	8.395	0.061	0.069	4.717	0.004	0.025	1.835	6.968	96.440	89.6
#110-4	0.962	0.044	36.332	15.638	23.407	0.000	9.445	0.035	0.000	4.304	0.045	0.031	1.132	4.394	95.363	90.7
#110-5	1.132	0.025	38.738	13.241	24.318	0.000	10.444	0.031	0.029	5.090	0.027	0.015	1.103	1.597	95.318	89.5
#110-6	1.079	0.030	34.603	16.175	23.069	0.000	8.389	0.038	0.000	4.608	0.074	0.098	1.712	6.819	96.256	89.9
#110-7	0.943	0.015	35.986	15.550	23.175	0.005	9.054	0.011	0.000	4.676	0.076	0.080	1.448	5.228	95.863	89.8
#110-8	1.087	0.001	39.158	13.143	23.943	0.000	10.282	0.022	0.047	4.844	0.073	0.056	1.190	1.579	94.967	89.8
#110-9	1.211	0.092	34.441	16.152	23.280	0.003	8.484	0.036	0.002	4.519	0.069	0.128	1.673	6.694	96.273	90.2
#110-10	1.040	0.047	36.715	15.316	23.334	0.000	9.092	0.119	0.000	4.844	0.056	0.017	1.476	4.482	96.100	89.6
#110-11	0.948	0.038	39.218	13.516	24.103	0.002	10.358	0.042	0.005	4.596	0.016	0.004	0.943	1.757	95.146	90.3
#110-12	1.034	0.025	38.406	14.766	24.334	0.011	9.192	0.044	0.038	3.748	0.000	0.000	0.621	3.039	94.856	92.1
#110-13	1.074	0.045	36.318	15.408	23.417	0.000	9.363	0.078	0.050	4.441	0.058	0.032	1.319	4.202	95.353	90.4
#110-14	1.037	0.004	38.603	13.710	24.682	0.002	10.091	0.075	0.035	4.841	0.067	0.000	0.980	1.807	95.496	90.1
#110-15	1.066	0.046	33.854	16.321	22.660	0.000	8.078	0.062	0.042	4.534	0.034	0.057	1.828	7.510	95.645	89.9
#110-16	1.082	0.061	36.276	15.347	23.328	0.000	9.228	0.065	0.046	4.465	0.029	0.079	1.472	4.610	95.640	90.3

Table 3. *Cont.*

Sample	F	Na$_2$O	SiO$_2$	Al$_2$O$_3$	MgO	Cl	K$_2$O	CaO	NiO	FeO	MnO	Cr$_2$O$_3$	TiO$_2$	BaO	Total	Mg$^\#$
#110-17	0.959	0.029	38.324	14.244	24.137	0.004	10.046	0.053	0.000	4.532	0.058	0.040	0.933	2.236	95.213	90.5
#110-18	0.978	0.063	36.343	15.407	23.025	0.004	9.492	0.118	0.060	4.238	0.045	0.069	1.349	4.391	95.170	90.7
#110-19	1.011	0.028	38.816	13.623	23.976	0.000	10.417	0.101	0.016	4.698	0.043	0.009	1.054	1.795	95.169	90.1
#110-20	1.036	0.079	36.535	15.347	23.586	0.008	9.425	0.075	0.059	4.552	0.067	0.032	1.256	4.435	96.052	90.2
#110-21	1.059	0.065	38.151	14.398	24.148	0.000	9.984	0.119	0.000	4.638	0.024	0.053	1.179	2.678	96.052	90.3
#110-22	0.941	0.057	37.042	15.115	23.663	0.000	9.456	0.043	0.040	4.390	0.043	0.025	1.242	3.863	95.525	90.6
#110-23	1.139	0.024	39.381	13.620	24.352	0.006	10.312	0.039	0.015	4.439	0.004	0.045	0.874	1.788	95.569	90.7
#110-24	1.081	0.035	33.889	16.543	22.425	0.008	7.968	0.112	0.000	4.654	0.059	0.082	1.918	8.000	96.322	89.6
#110-25	1.187	0.007	36.293	15.067	22.888	0.003	9.165	0.088	0.043	4.787	0.048	0.111	1.499	4.617	95.300	89.5
#110-26	1.107	0.000	38.377	14.317	23.915	0.000	9.801	0.159	0.028	4.597	0.074	0.048	1.062	2.614	95.634	90.3
#110-27	0.971	0.032	35.742	15.442	23.005	0.009	8.971	0.126	0.000	5.197	0.048	0.081	1.576	5.190	95.978	88.8
#110-28	1.084	0.019	37.055	14.940	23.509	0.000	9.648	0.101	0.032	4.733	0.072	0.072	1.408	3.487	95.721	89.9
#110-29	1.023	0.010	36.524	15.773	23.532	0.006	9.326	0.138	0.000	4.688	0.037	0.001	1.235	4.159	96.030	90.0
#110-30	1.030	0.056	36.791	15.277	23.454	0.004	9.464	0.025	0.053	4.315	0.041	0.020	1.086	4.374	95.567	90.7
#110-31	0.928	0.029	38.614	14.608	24.714	0.000	9.850	0.052	0.011	4.297	0.122	0.024	0.583	2.711	96.154	91.1
#110-32	0.890	0.054	36.630	15.350	23.427	0.006	9.431	0.071	0.000	4.794	0.078	0.017	1.298	4.398	96.099	89.7
#110-33	0.997	0.055	36.715	15.474	24.021	0.000	9.279	0.203	0.009	4.555	0.036	0.056	1.077	3.738	95.794	90.4
#110-34	1.193	0.066	34.839	16.190	22.540	0.000	8.152	0.045	0.032	5.212	0.052	0.114	1.844	6.294	96.082	88.5

6. Discussion

6.1. Origin of the #50 Phlogopite Zone

The process of magmatic evolution has always been a hot topic. The phlogopite from Southern Liaoning kimberlite has very complex zone structures, especially #50 phlogopite. It is believed that the zone structure of phlogopite can record the process of magmatic evolution. Therefore, this study will analyze the complex origin of phlogopite #50.

6.1.1. Origin of #50 Low-Ti-Cr Phlogopite Cores

Zonation is a prevalent feature in phlogopite from the kimberlite area in southern Liaoning. The cores of phlogopite generally have resorption (i.e., embayment, rounded shape) and deformation textures [14,28]. Furthermore, the compositions of the majority of the phlogopite macrocryst cores observed in kimberlite samples from southern Liaoning exhibit a broad similarity to those found in mantle-derived xenoliths from Kimberley and other kimberlites in southern Africa (Figure 6A,C,E). This implies that there is a possibility of their shared origin, indicating that these phlogopite cores are derived from the disaggregation of metasomatized mantle rocks entrained by kimberlite magmas [23,28,47], as previously inferred for olivine [30,60,61] and spinel [62] in kimberlites. Therefore, these cores are xenocrystic and do not crystallize directly from the host-kimberlite magma [9].

Based on the limited compositional changes observed in the macrocryst cores of the low-Ti-Cr (xenocrystic) samples, it can be inferred that the mantle source rock may have undergone similar metasomatic events. The phlogopite macrocrysts exhibit a compositional variation from xenocrystic cores with low Ti-Cr contents to inner rims with high Ti-Cr contents, accompanied by a decrease in Mg$^\#$ and an increase in the contents of Al and Ba. This results in the typical zoned structure observed in the phlogopite macrocrysts from southern Liaoning. These observations, in combination with the embayments and deformation structures in the macrocryst cores of phlogopite, suggest that the low-Ti-Cr xenocrystic cores cannot have existed stably at any stage of the evolution of the kimberlite magma.
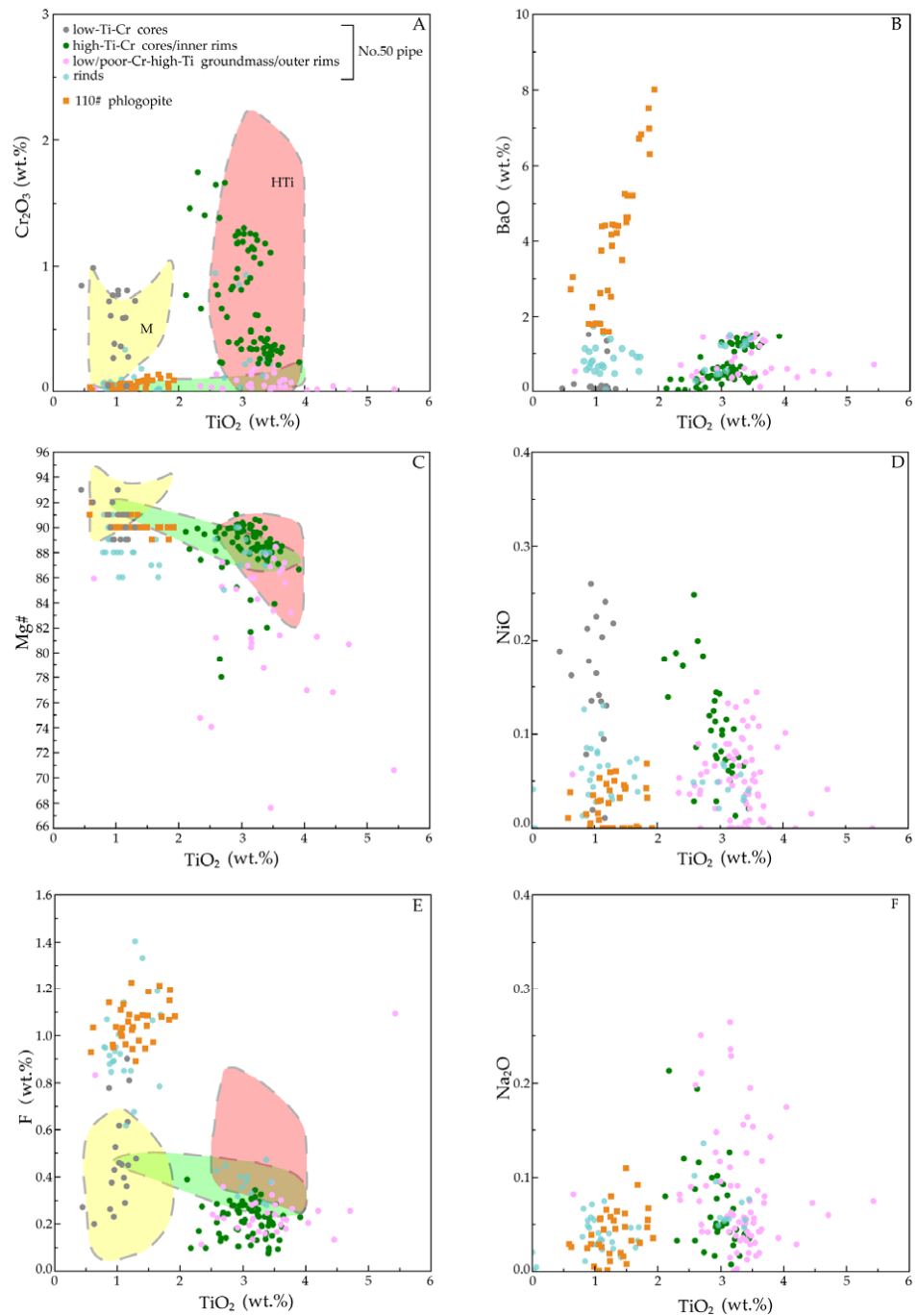
Figure 6. Major element variation diagrams for phlogopite from southern Liaoning kimberlites. (**A**,**C**,**E**) The light-yellow field "M" shows the composition of phlogopite from metasomatized peridotite xenoliths; the light-green field shows the composition of phlogopite from kimberlite groundmass; the light-pink field "HTi" shows the composition of high-Ti-Cr phlogopite from mantle xenoliths, including polymictic breccia (modified from Kargin et al., 2019) [63]. (**B**,**D**,**F**) are major oxide co-variation diagrams for phlogopite grains from the southern Liaoning kimberlites.

Altered minerals (as shown in Figures 3 and 4, with talc and serpentine as examples) were observed within the cores, where deformation features, cleavage development, and crystal distortion were commonly present. The formation of metasomatic minerals may occur after the entrapment of the phlogopite macrocrystic core (xenocryst) by the kimberlite-like magma. Based on petrographic observations, both talc and serpentine are present in the macrocryst cores, whereas no serpentine or talc is found at the edges of the cores. If the

metasomatic event involving hydrothermal (H_2O-rich fluid/melt) occurred before capture by the magma, why are the edges of the low-Ti-Cr xenocrystic cores not affected, and why do metasomatic minerals occur only in the cores? We hypothesize that the outer margins of the phlogopite developed a sequence of high-Ti-Cr and low-Cr/Cr-poor inner and outer rims (as described below) after the entrapment of the low-Ti-Cr xenocrystic cores by the kimberlite-like magma and that these rims protected the cores. Therefore, we propose that the metasomatic event occurred after xenocryst entrapment by the kimberlite magma, most likely during the later magmatic stage. The hydrothermal (fluid/melt) process induced metasomatism of the cores and produced altered minerals (e.g., serpentine and talc) along deformed and twisted cleavage planes. The variable composition of the rinds appears to lend support to this concept (discussed below).

6.1.2. Origin of the #50 High-Ti-Cr Phlogopite Cores/Inner Rims

The high-Ti-Cr cores/inner rims of phlogopite in the kimberlite samples from southern Liaoning exhibit similarity to both the polymictic breccia matrix and overgrowths in mantle xenoliths, suggesting a possible common origin (Figure 6). The entrained polymictic breccias are considered "failed" kimberlite emplacements; these early kimberlite-like melts rapidly intruded and were retained in the lithospheric mantle, and fragments were subsequently transported to the surface by kimberlite magma pulses [59,64]. The phlogopite in the polymictic breccia matrix and the phlogopite overgrowths in the mantle xenoliths have previously been interpreted as having crystallized from kimberlite-related melts [59,65]. We suggest a similar origin for the high-Ti-Cr zones of the #50 phlogopite macrocrysts in southern Liaoning.

The high-Ti-Cr phlogopite is the product of the interaction between mantle rocks and kimberlitic magmas at mantle depths or crystallized directly from stalled batches of kimberlitic magmas ("failed" kimberlites) at mantle depths [9,63]. High-Ti-Cr phlogopite is thought to be derived from less fractionated kimberlite melts, which have been extensively modified by interactions with refractory mantle peridotite wall rocks [23,66]. The enrichment of Cr, Ni and Mg in the high-Ti-Cr phlogopite (cores/inner rims) is evidence of mantle peridotite assimilation by kimberlite magma at lithospheric mantle depths [23], which plays a buffering role in the evolution of the groundmass phlogopite composition (Mg depletion and Al and Ba enrichment in the low-Cr/Cr-poor phlogopite).

The high-Ti-Cr zone manifests in two primary forms: either as inner rims exhibiting resorption phenomena and overgrowing the low-Ti-Cr xenocrystic cores or as a core containing both euhedral and embayed textures. Compared with the low-Ti-Cr (xenocrystic) cores, high-Ti-Cr phlogopite shows a slight but stable depletion in Mg, but Fe, Ti and Al are more enriched.

The euhedral high-Ti-Cr cores and high-Ti-Cr inner rims/cores with resorption phenomena may represent distinct crystallization environments. First, the preservation of euhedral high-Ti-Cr cores implies formation in a relatively stable and balanced mantle environment prior to being entrapped by late-stage kimberlite magma and emplaced at the Earth's surface. These cores may represent crystals that directly precipitated from kimberlite melts that stagnated at great depths within the mantle. Second, the high-Ti-Cr inner rims/cores with resorption textures may have experienced interference from different batches of pulsed kimberlite melts. This compositional zone could exhibit an unbalanced phase (as evidenced by the embayed textures) associated with the pulsed eruption of kimberlite magmas, which is supported by discrete compositional changes. Petrographic observations can also be utilized to clarify this issue. In the matrix where high-Ti-Cr crystals occur, a distinct heterogeneity in the kimberlite matrix is observed (Figure 2C). This suggests that the formation of these high-Ti-Cr phlogopite zones with resorption phenomena is in an unbalanced stage with magma, and it is believed that later pulsed magma played a crucial role until it reached the surface. These phenomena are indicative of the complex and perturbed formation environment in which high-Ti-Cr phlogopite formed. It is widely acknowledged that kimberlite pipes are formed through a series of discon-

tinuous volcanic activities, which might result in the formation of distinct units within a single diatreme [11–13]. This is in line with the complex zonal pattern observed through microscopic analysis and discrete compositional variations, indicating the occurrence of multistage kimberlite magmatic pulses.

6.1.3. Origin of #50 Low-Cr/Cr-Poor Phlogopite Outer Rims

The low-Cr/Cr-poor zones of the #50 phlogopite are typically observed as the outer rims of crystals, which constitute a significant portion of the phlogopite zone in the region. In the process of magmatic emplacement, the magmatic composition undergoes continuous evolution due to magmatic fractionation and assimilation, as well as contamination by crustal wall rocks. The low-Cr/Cr-poor outer rims are rich in Al, Ba, Ti, F, Zr and Nb and depleted in Mg, Cr, Sr and Ni; this pattern is consistent with the composition of groundmass phlogopite grains crystallized directly from the host-kimberlite magma [4,21,23,26,63]. Cr-spinel inclusions occur frequently within the zone, suggesting that the majority of the zone was formed after Cr-spinel fractionation, which aligns with the low chromium content characteristics exhibited by the zone [23,67]. However, spinel inclusions also appear in the high-Ti-Cr zone (Figure 4). Therefore, differentiation via Cr-spinel crystallization may not be the sole cause of the presence of low-Cr/Cr-poor outer rims. Due to the significant variation in the composition of the low-Cr/Cr-poor rims, particularly characterized by the extreme depletion of Cr and enrichment of Ti, the progressive decrease in V/Sc ratios is combined with the decreasing Ni levels in the low-Cr/Cr-poor phlogopite (Figure 7l) to document an increase in the oxygen fugacity ratio (fO_2) [68]; this increase in fO_2 could be one of the factors contributing to the influx of Ti from residual magma into the zone in significant quantities [69]. Furthermore, considering the resemblance of the high-Ti-Cr zone to magmatic mica in polymictic breccias and mica overgrowths found in other mantle xenoliths, it is plausible that the high-Ti-Cr zone crystallized within the mantle environment and might have been influenced by intermittent injections of early kimberlite magma. Phlogopite is considered a magmatic mineral in kimberlite magmas, and the crystallization process may begin in the lithospheric mantle and continue into the crust [9,23]. The conditions for phlogopite crystallization are limited to pressures of <20 kbar and are most conducive to formation at ~10 kbar, i.e., in the crust [70]. The low-Cr/Cr-poor zone, as the outermost zone of phlogopite, and its similarity to groundmass phlogopite in composition suggest that it was formed in a near-crustal environment [9]. Based on the distinct crystallization environments, these minerals may not have originated from the same batch of melted pulses [9].

Furthermore, a partial evolutionary trend toward the composition of biotite can be observed in the low-Cr/Cr-poor outer rims of the #50 phlogopite (Figure 8). Al-rich biotite megacrysts (type I biotite) surrounded by late groundmass mica were found for the first time in mica kimberlites in South Africa (Swartruggens, Saltpeerpan and Monteleo) and Canada (Upper Canada Mine, Ontario) [71]. Phlogopite-related biotite megacrysts have also been found in the group II kimberlite New Elands, Sover Mine, Bellsbank, South Africa [26]. The occurrence of closely related phlogopite–biotite megacrysts has also been documented in the Mengyin kimberlite. It is speculated that the appearance of these megacrysts is related to metasomatic metamorphism of the wall rock during the late magmatic transformation or ascent, and such megacrysts may have formed through the reaction of an H_2O-CO_2-rich fluid (or melt) in the late magmatic period with nearby iron-rich wall rock or crustal xenoliths [69].
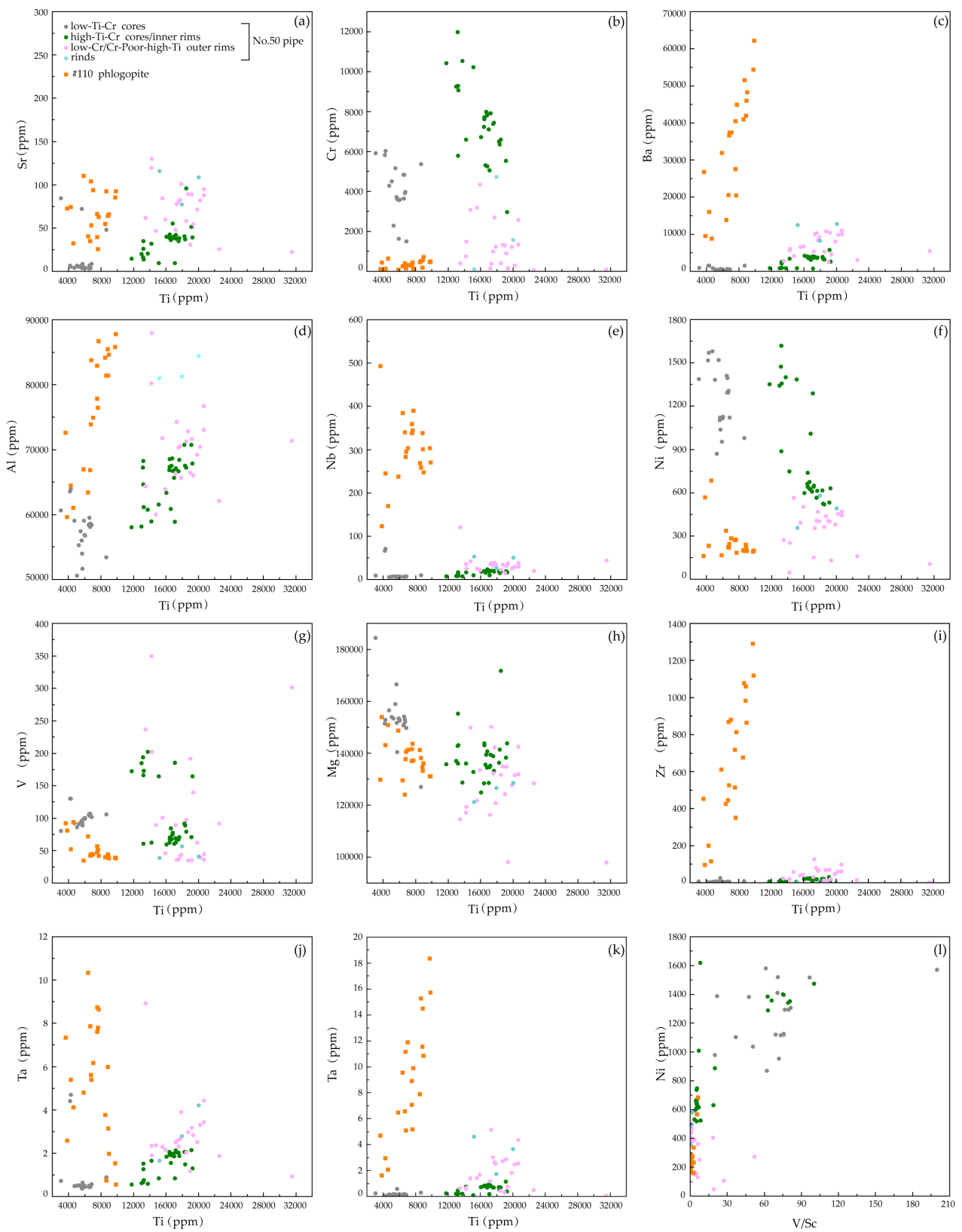
Figure 7. (**a**–**l**) Trace element covariation diagrams for phlogopite grains from the southern Liaoning kimberlite.
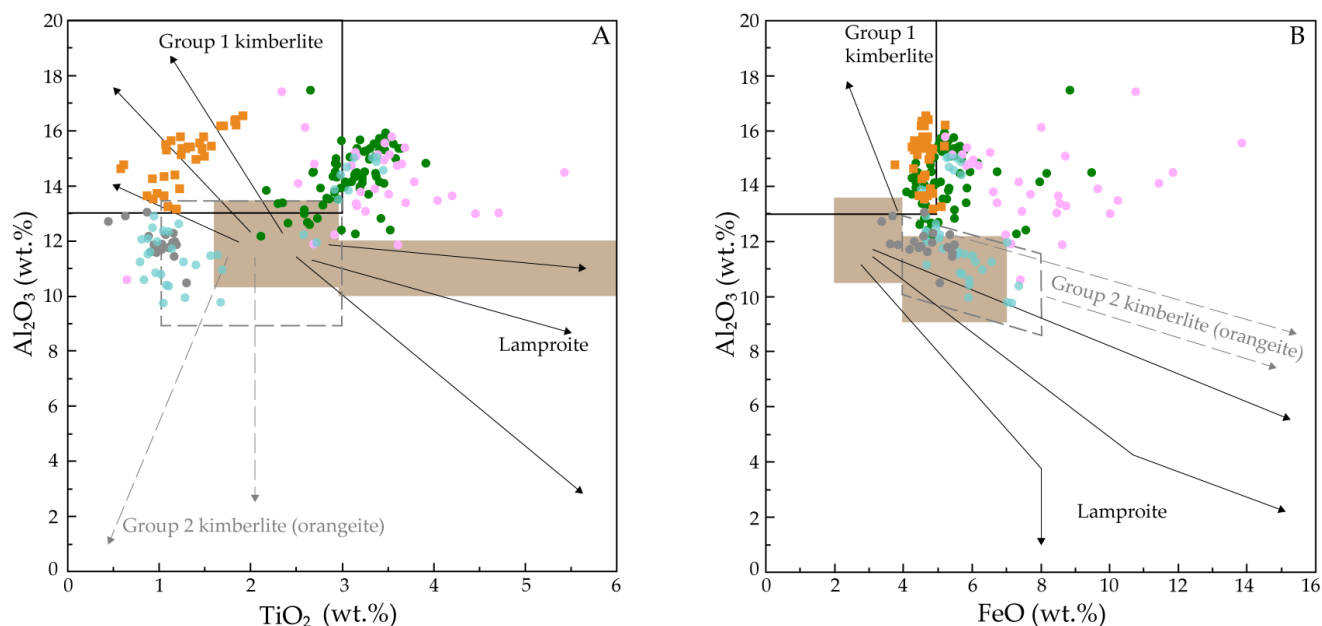
Figure 8. Evolutionary trends in the composition of groundmass micas are indicated for lamproite (brown shaded fields and labeled continuous black lines), Group II kimberlites (orangeites; dashed box and light gray lines), and Group I kimberlite (labeled box and continuous black lines) (modified from Downes et al., 2006) [23]. (**A**) Al_2O_3 (wt%) vs. TiO_2(wt%); (**B**) Al_2O_3 (wt%) vs. FeO(wt%).

6.1.4. Origin of the #50 Phlogopite Rinds

The rinds are extremely narrow and challenging to discern. X-ray elemental maps initially revealed the presence of the #50 phlogopite rinds in the outermost layer of certain phlogopite crystals (Figure 3). An obvious feature of the rinds is the re-enrichment of Mg. Based on the origin of olivine rinds [34], crystallization from residual kimberlite melt under high oxygen fugacity conditions is suggested [33,70,72,73]. Notably, the rinds of the #50 phlogopite exhibit two distinct compositional ranges, namely, low-Ti-Cr rinds (designated rind I) and high-Ti-Cr rinds (designated rind II). We propose that the formation of rind I (low-Ti-Cr rinds) is attributed to melting depletion during the late stages of magmatic evolution. The differentiation of crystallization should be considered the primary factor leading to the depletion of residual melt.

Rind II with high-Ti-Cr component characteristics appears somewhat abruptly in crystals with rinds. However, we posit that the presence of this composition is not random and that it substantiates the longstanding conjecture regarding a hydrothermal (H_2O-rich fluids) superimposition event during the late magmatic evolution of the No. 50 pipe kimberlite. The overlapping of late hydrothermal processes involving H_2O-rich fluids may account for the abnormal increase in Cr concentrations observed in some rinds II. The hydrothermal fluid infiltrated the phlogopite cores through cleavage planes, causing metasomatism in the xenocrystic cores and resulting in the formation of metasomatic minerals such as serpentine and talc (part 6.1 above; Figures 3 and 4). The diverse range of rinds illustrates the complex nature of the environment during the later stages of magmatic evolution. In addition, we hypothesize that another factor contributing to maintaining a high Ti concentration was an increase in oxygen fugacity during the crystallization process in near-surface environments. This led to a significant influx of Ti from the melt into rind II, resulting in an anomalously enriched Ti concentration [74]. Similar to the origin of low-Cr/Cr-poor phlogopite, this explanation is also consistent with the Mg enrichment of the rinds.

A plausible conjecture here is that rind I might not have formed simultaneously with rind II, albeit direct evidence to substantiate this claim is lacking. It is speculated that under high oxygen fugacity conditions, a large amount of Ti in the residual magma entered rind

II, which led to further loss of Ti from the residual magma; subsequently, rind I may have formed in this environment. Rind II may have crystallized simultaneously or slightly later than the low-Cr/Cr-poor outer rims and before rind I.

6.2. Origin of the #110 Phlogopite

Although zonation can also be observed in BSE images, the #110 phlogopite has a more homogeneous composition and does not exhibit zoning as complex as that of the #50 phlogopite. No rinds were found in the outermost layer. The #110 phlogopite has similar compositional characteristics to rind I, such as enrichment of Mg and F. In the Aries kimberlite (Central Kimberley Basin, Western Australia), the presence of rare Mg-F-rich phlogopite in this macrocrystic phlogopite kimberlite (MPK) was previously reported. It is believed to have originated from the crystallization of a carbonate-rich melt or an H_2O-CO_2 fluid interacting with highly refractory peridotite [23]. In addition, the #110 phlogopite has higher Al and Ba contents. Kimberlites on the Terskii coast of Russia [75], the Iron Hill carbonatites [21] and the Jacupiranga carbonatites from Brazil [76] are also reported to contain Ba-rich phlogopite. Phlogopite is the main carrier of Ba in the upper mantle, and high-Ba phlogopite has been found in peridotite xenoliths in the kimberlite in Jagersfontein, South Africa; this phlogopite is believed to be the product of mantle metasomatism [69]. The #110 phlogopite has $Mg^{\#}$ values similar to those of the #50 phlogopite xenocryst core and high-Ti-Cr cores/inner rims, which also indicates that the #110 phlogopite formed in a mantle environment. However, due to its euhedral morphology and limited compositional changes, it is more likely to have undergone direct crystallization from the magma rather than being of xenocrystic origin.

6.3. Lithology Determination of Pipe Nos. 50 and 110 Kimberlites

The specific rock properties of the kimberlite in southern Liaoning have not been discussed in detail, while the composition characteristics of phlogopite can restrict the attribution of the kimberlite. In contrast to the Mengyin diamond area situated in the NCC, no discernible evolutionary pattern of tetraferriphlogopite was observed in this investigation [69], while enrichment of both Fe and Al in #50 phlogopite is an identifying characteristic of kimberlites [26,77]. The behavior of the #50 phlogopite in this study is somewhat similar to that of the Tongo micaceous kimberlite from the Man Craton, West Africa [68], and Aries micaceous kimberlite from the Central Kimberley Basin, Western Australia [23]. For instance, (1) both samples exhibit a high abundance of mica; (2) the majority of phlogopite displays simultaneous Fe and Al enrichment, which is considered a typical characteristic of kimberlites; and (3) no diopside has been observed in the petrographic analysis. The difference is that the carbonate in the Tongo kimberlite is dolomite, while the carbonate in the Liaoning No. 50 pipe kimberlite is calcite. This reflects the special characteristics of the southern Liaoning kimberlite. Because the evolution trend of the #50 phlogopite is similar to that of the Tongo and Aries micaceous kimberlites and there are no obvious lamprophyre features, the No. 50 pipe kimberlite is classified as a micaceous kimberlite. In contrast, the No. 110 pipe kimberlite may exhibit a closer affinity to Group I kimberlite.

6.4. Kimberlite Emplacement Mechanism

The occurrence of the complex phlogopite zone in the kimberlites in southern Liaoning suggests that the emplacement of the kimberlite melt into the lithospheric mantle took place intermittently during multiple episodes. The mantle-derived xenoliths (polymictic breccias) of magmas that failed to emplace as true kimberlites, the crystalline environment of the high-Ti-Cr cores/inner rims and the complexity of the low-Cr/Cr-poor and rinds may record repeated, pulsed kimberlite emplacement events. Although carbonate-rich kimberlite melts rise faster, the melts of the early pulses did not easily reach the surface because of the strong reaction between these melts and mantle rocks and were more likely to stagnate (crystallize) in the deep mantle [78–82]. This study proposes that the early

eruption of kimberlite melt occurred along tectonic fractures and rock fissures through a repeated emplacement process. The strong interaction between the kimberlite magma and the channel wall rock led to the formation of a metasomatically transformed magma channel resembling protective film-like structures. The reactivity between the subsequent kimberlite melt and the wall rock was significantly diminished during its passage through the conduit, resembling a desensitization effect. This enabled subsequent ascending melts to maintain a rapid eruption rate and achieve successful emplacement at the surface [59], indicating that successful kimberlite magma emplacement at the Earth's surface requires multiple stages of magmatic activity and a magma conduit altered by kimberlite-like melts [9,63]. The complex zonal structures of the phlogopite in the southern Liaoning kimberlite provide evidence for the significant role played by the multistage pulsed emplacement of the kimberlite magma in both its evolution and final mineral composition.

7. Conclusions

The formation of high-Ti-Cr phlogopite is thought to involve the assimilation of mantle rock by kimberlite magma at mantle depths, suggesting that kimberlite emplacement failure may be a relatively common phenomenon. These failed kimberlite melts stopped deep in the mantle and were later entrained and carried to the surface by kimberlite melts during subsequent multistage activity.

Furthermore, there is a partial evolutionary trend toward the composition of biotite in the low-Cr/Cr-poor outer rims of the #50 phlogopite. It is speculated that the appearance of phlogopite and biotite is related to the metasomatic metamorphism of the wall rock during the late magmatic transformation or ascent and that these minerals may have formed by the reaction of the H_2O- and CO_2-rich fluid (or melt) in the late magmatic period with nearby iron-rich wall rock or crustal xenoliths.

This initial report documented the presence of phlogopite rinds in kimberlite in Liaoning Province. The rinds of phlogopite #50 show two compositional characteristics: (1) rind I features low Ti-Cr contents, and (2) rind II features high Ti-Cr contents. Mg re-enrichment occurs in the rinds and is indicative of an increase in oxygen fugacity. It is proposed that rind II may have formed prior to rind I, with rind II potentially undergoing crystallization simultaneously or slightly later than the low-Cr/Cr-poor outer rims. In the high oxygen fugacity environment, a large amount of Ti in the residual magma entered rind II, resulting in further loss of Ti in the residual magma, and rind I then formed at this time. The complex alterations observed in the #50 phlogopite rinds are indicative of the complexity and volatility of the environment during the later stages of magmatic evolution. The presence of serpentine and talc minerals in the low-Ti-Cr cores (xenocrysts) may serve as evidence for hydrothermal metasomatism.

The compositions of the different zones in the #110 phlogopite are very homogeneous, and the #110 phlogopite is more enriched in Ba. High-Ba phlogopite is believed to be the product of mantle metasomatism. Based on the Mg and F enrichment in the #110 phlogopite, the formation of this mineral likely occurred through the interaction of a carbonate-rich melt or H_2O-CO_2 fluid with refractory peridotite. In addition, due to its euhedral morphology and limited compositional changes, this phlogopite is more likely to have crystallized directly from the magma than to be of xenocrystic origin.

The #50 phlogopite generally exhibits the characteristic trend of concurrent enrichment in both Al and Fe, which is a typical feature of kimberlite rocks. The characteristics of the #50 phlogopite in this study are somewhat similar to those of the Tongo micaceous kimberlite (Man Craton, West Africa) and Aries micaceous kimberlite (Central Kimberley Basin, Western Australia). Thus, the diamond host rock in the No. 50 pipe is also tentatively called micaceous kimberlite.

Because kimberlite melts are prone to strong reactions with mantle wall rocks, the magma channel underwent a transformation due to kimberlite magmatic metasomatism during the early magmatic pulses. Consequently, a protective layer of wall rock formed on the surface of the magma channel, thereby reducing the interaction between subsequent

kimberlite magma and the surrounding mantle rocks. This process ultimately facilitated the successful emplacement of later kimberlite magma along the transformed channel.

In this study, phlogopite was utilized as a medium for the first time in the southern Liaoning kimberlite region. Through detailed analysis of the geochemical characteristics of phlogopite crystals, new evidence has been provided for the multistage pulsed emplacement mechanism and lithologic determination of kimberlite magma. Additionally, new constraints on the evolution of kimberlite magmas have also been established.

References

1. Becker, M.; Le Roex, A.P. Geochemistry of South African on- and off-craton, group I and group II kimberlites: Petrogenesis and source region evolution. *J. Petrol.* **2006**, *47*, 673–703. [CrossRef]
2. Giuliani, A.; Pearson, D.G.; Soltys, A.; Dalton, H.; Phillips, D.; Foley, S.F.; Lim, E.; Goemann, K.; Griffin, W.L.; Mitchell, R.H. Kimberlite Genesis from a Common Carbonate-Rich Primary Melt Modified by Lithospheric Mantle Assimilation. 2020. Available online: http://advances.sciencemag.org/ (accessed on 12 December 2022).
3. Le Roex, A.P.; Bell, D.R.; Davis, P. Petrogenesis of group I Kimberlites from Kimberley, South Africa: Evidence from bulk-rock geochemistry. *J. Petrol.* **2003**, *44*, 2261–2286. [CrossRef]
4. Mitchell, R.H. *Kimberlites, Mineralogy, Geochemistry, and Petrology*; Springer Science & Business Media: Berlin/Heidelberg, Germany, 1989.
5. Woodhead, J.; Hergt, J.; Giuliani, A.; Maas, R.; Phillips, D.; Pearson, D.G.; Nowell, G. Kimberlites reveal 2.5-billion-year evolution of a deep, isolated mantle reservoir. *Nature* **2019**, *573*, 578–581. [CrossRef] [PubMed]
6. Coe, N.; Roex, A.; Gurney, J.; Pearson, G.D.; Nowell, G. Petrogenesis of the Swartruggens and Star Group II kimberlite dyke swarms, South Africa: Constraints from whole rock geochemistry. *Contrib. Mineral. Petrol.* **2008**, *156*, 627–652. [CrossRef]
7. Giuliani, A.; Phillips, D.; Woodhead, J.D.; Kamenetsky, V.S.; Fiorentini, M.L.; Maas, R.; Soltys, A.; Armstrong, R.A. Did diamond-bearing orangeites originate from MARID-veined peridotites in the lithospheric mantle? *Nat. Commun.* **2015**, *6*, 6837. [CrossRef] [PubMed]
8. Nowell, G.M.; Pearson, D.G.; Bell, D.R.; Carlson, R.W.; Smith, C.B.; Kempton, P.D.; Noble, S.R. Hf isotope systematics of kimberlites and their megacrysts: New constraints on their source regions. *J. Petrol.* **2004**, *45*, 1583–1612. [CrossRef]
9. Giuliani, A.; Phillips, D.; Kamenetsky, V.S.; Goemann, K. Constraints on kimberlite ascent mechanisms revealed by phlogopite compositions in kimberlites and mantle xenoliths. *Lithos* **2016**, *240–243*, 189–201. [CrossRef]
10. Dawson, J.B.; Hawthorne, J.B. Intrusion Features of Some Hypabyssal South African Kimberlites. *Bull. Volcanol.* **1970**, *34*, 740–757. [CrossRef]
11. Field, M.; Scott Smith, B.H. Contrasting Geology and Near-Surface Emplacement of Kimberlite Pipes in Southern Africa and Canada. In *Extended Abstracts, Proceedings of the 7th International Kimberlite Conference, Cape Town, South Africa, 11–17 April 1998*; Gurney, J.J., Pascoe, M.D., Richardson, S.H., Eds.; Red Roof Design: Cape Town, South Africa, 1999; pp. 214–237.
12. Nowicki, T.; Crawford, B.; Dyck, D.; Carlson, J.; McElroy, R.; Oshust, P.; Helmstaedt, H. The geology of kimberlite pipes of the Ekati property, Northwest Territories, Canada. *Lithos* **2004**, *76*, 1–27. [CrossRef]

13. Sparks, R.S.J. Kimberlite volcanism. *Annu. Rev. Earth Planet Sci.* **2013**, *41*, 497–528. [CrossRef]
14. Clement, C.R. A Comparative Geological Study of Some MajorKimberlite Pipes in the Northern Cape and Orange Free State. Ph.D. Thesis, University of Cape Town, Cape Town, South Africa, 1982.
15. Brooker, R.A.; Sparks, R.S.J.; Kavanagh, J.L.; Field, M. The volatile content of hypabyssal kimberlite magmas: Some constraints from experiments on natural rock compositions. *Bull. Volcanol.* **2011**, *73*, 959–981. [CrossRef]
16. Kamenetsky, M.B.; Sobolev, A.V.; Kamenetsky, V.S.; Maas, R.; Danyushevsky, L.V.; Thomas, R.; Pokhilenko, N.P.; Sobolev, N.V. Kimberlite melts rich in alkali chlorides and carbonates: A potent metasomatic agent in the mantle. *Geology* **2004**, *32*, 845–848. [CrossRef]
17. Kamenetsky, V.S.; Golovin, A.V.; Maas, R.; Giuliani, A.; Kamenetsky, M.B.; Weiss, Y. *Towards a New Model for Kimberlite Petrogenesis: Evidence from Unaltered Kimberlites and Mantle Minerals. Earth-Science Reviews*; Elsevier: Amsterdam, The Netherlands, 2014; pp. 145–167. [CrossRef]
18. Nielsen, T.F.D.; Sand, K.K. The Majuagaa kimberlite dike, Maniitsoq region, West Greenland: Constraints on an Mg-rich silicocarbonatitic melt composition from groundmass mineralogy and bulk compositions. *Can. Mineral.* **2008**, *46*, 1043–1061. [CrossRef]
19. Patterson, M.; Francis, D.; McCandless, T. Kimberlites: Magmas or mixtures? *Lithos* **2009**, *112*, 191–200. [CrossRef]
20. Tappe, S.; Foley, S.F.; Jenner, G.A.; Heaman, L.M.; Kjarsgaard, B.A.; Romer, R.L. Genesis of ultramafic lamprophyres and carbonatites at Aillik Bay, Labrador: A consequence of incipient lithospheric thinning beneath the North Atlantic Craton. *J. Petrol.* **2006**, *47*, 1261–1315. [CrossRef]
21. Reguir, E.P.; Chakhmouradian, A.R.; Halden, N.M.; Malkovets, V.G.; Yang, P. Major- and trace-element compositional variation of phlogopite from kimberlites and carbonatites as a petrogenetic indicator. *Lithos* **2009**, *112*, 372–384. [CrossRef]
22. Larionova, Y.O.; Sazonova, L.V.; Lebedeva, N.M.; Nosova, A.A.; Tretyachenko, V.V.; Travin, A.V.; Kargin, A.V.; Yudin, D.S. Kimberlite age in the Arkhangelsk Province, Russia: Isotopic geochronologic Rb–Sr and 40Ar/39Ar and mineralogical data on phlogopite. *Petrology* **2016**, *24*, 562–593. [CrossRef]
23. Downes, P.J.; Wartho, J.A.; Griffin, B.J. Magmatic evolution and ascent history of the Aries micaceous kimberlite, central Kimberley Basin, Western Australia: Evidence from zoned phlogopite phenocrysts, and UV laser 40Ar/39Ar analysis of phlogopite-biotite. *J. Petrol.* **2006**, *47*, 1751–1783. [CrossRef]
24. Fritschle, T.; Prelević, D.; Foley, S.F.; Jacob, D.E. Petrological characterization of the mantle source of Mediterranean lamproites: Indications from major and trace elements of phlogopite. *Chem. Geol.* **2013**, *353*, 267–279. [CrossRef]
25. Hunren, R.H.; Kissi-Tng, R.D.; Tnvlon, L.A. Mid-to Late-Stage Kimberlitic Melt Evolution: Phlogopites and Oxides from the Fayette County Kimberlite, Pennsylvania. American Mineralogist 1984. Available online: http://pubs.geoscienceworld.org/msa/ammin/article-pdf/69/1-2/30/4216842/am69_30.pdf (accessed on 27 November 2020).
26. Mitchell, R.H. *Kimberlites, Orangeites, and Related Rocks. Kimberlites, Orangeites, and Related Rocks*; Springer: Berlin/Heidelberg, Germany, 1995. [CrossRef]
27. O'Brien, H.E.; Irving, A.J.; Stewear McCallum, I. Cornplex zoning and resorption of phenocrysts in mixed potassic mafic magmas of the Highwood Mountains, Montana. *Am. Mineral.* **1988**, *73*, 1007–1024.
28. Shee, S.R.; Bristow, J.W.; Shee, P.B.S.; Bell, D.R. The Petrogenesis of the Wesselton Mine Kimberlites, Kimberley, Cape Province, R.S.A. Ph.D. Thesis, University of Cape Town, Cape Town, South Africa, 1985; p. 220.
29. Sobolev, N.V.; Logvinova, A.M.; Zedgenizov, D.A.; Pokhilenko, N.P.; Malygina, E.V.; Kuzmin, D.V.; Sobolev, A.V. Petrogenetic significance of minor elements in olivines from diamonds and peridotite xenoliths from kimberlites of Yakutia. *Lithos* **2009**, *112*, 701–713. [CrossRef]
30. Sobolev, N.V.; Sobolev, A.V.; Tomilenko, A.A.; Kovyazin, S.V.; Batanova, V.G.; Kuz'min, D.V. Paragenesis and complex zoning of olivine macrocrysts from unaltered kimberlite of the Udachnaya-East pipe, Yakutia: Relationship with the kimberlite formation conditions and evolution. *RGG* **2015**, *56*, 260–279. [CrossRef]
31. Howarth, G.H. Olivine megacryst chemistry, Monastery kimberlite: Constraints on the mineralogy of the HIMU mantle reservoir in southern Africa. *Lithos* **2018**, *314–315*, 658–668. [CrossRef]
32. Howarth, G.H.; Gross, J. Diffusion-controlled and concentric growth zoning revealed by phosphorous in olivine from rapidly ascending kimberlite magma, Benfontein, South Africa. *Geochim. Cosmochim. Acta* **2019**, *266*, 292–306. [CrossRef]
33. Howarth, G.H.; Taylor, L.A. Multi-stage kimberlite evolution tracked in zoned olivine from the Benfontein sill, South Africa. *Lithos* **2016**, *262*, 384–397. [CrossRef]
34. Giuliani, A. Insights into kimberlite petrogenesis and mantle metasomatism from a review of the compositional zoning of olivine in kimberlites worldwide. *Lithos* **2018**, *312–313*, 322–342. [CrossRef]
35. Tovey, M.; Giuliani, A.; Phillips, D.; Moss, S. Controls on the explosive emplacement of diamondiferous kimberlites: New insights from hypabyssal and pyroclastic units in the Diavik mine, Canada. *Lithos* **2020**, *360*, 105410. [CrossRef]
36. Mitchell, R.H.; Giuliani, A.; O'Brien, H. What is a kimberlite? Petrology and mineralogy of hypabyssal kimberlites. *Elements* **2019**, *15*, 381–386. [CrossRef]
37. Yang, Y.H.; Wu, F.Y.; Wilde, S.A.; Liu, X.M.; Zhang YBin Xie, L.W.; Yang, J.H. In situ perovskite Sr-Nd isotopic constraints on the petrogenesis of the Ordovician Mengyin kimberlites in the North China Craton. *Chem. Geol.* **2009**, *264*, 24–42. [CrossRef]

38. Donnelly, C.L.; Griffin, W.L.; Yang, J.H.; O'Reilly, S.Y.; Li, Q.L.; Pearson, N.J.; Li, X.H. In situ U-Pb dating and Sr-Nd isotopic analysis of perovskite: Constraints on the age and petrogenesis of the Kuruman Kimberlite Province, Kaapvaal Craton, South Africa. *J. Petrol.* **2012**, *53*, 2497–2522. [CrossRef]

39. Sarkar, C.; Storey, C.D.; Hawkesworth, C.J. Using perovskite to determine the pre-shallow level contamination magma characteristics of kimberlite. *Chem. Geol.* **2014**, *363*, 76–90. [CrossRef]

40. Zhu, R.Z.; Ni, P.; Ding, J.Y.; Wang, G.G.; Fan, M.S.; Li, S.N. Metasomatic processes in the lithospheric mantle beneath the No. 30 kimberlite (Wafangdian region, North China craton). *Can. Miner.* **2019**, *57*, 499–517. [CrossRef]

41. Zhu, R.Z.; Ni, P.; Ding, J.Y.; Wang, D.Z.; Ju, Y.; Kang, N.; Wang, G.G. Petrography, chemical composition, and Raman spectra of chrome spinel: Constraints on the diamond potential of the No. 30 pipe kimberlite in Wafangdian, North China Craton. *Ore Geol. Rev.* **2017**, *91*, 896–905. [CrossRef]

42. Hoare, B.C.; O'Sullivan, G.; Tomlinson, E.L. Metasomatism of the Kaapvaal Craton during Cretaceous intraplate magmatism revealed by combined zircon U-Pb isotope and trace element analysis. *Chem. Geol.* **2021**, *578*, 120302. [CrossRef]

43. Veglio, C.; Lawley, C.J.M.; Pearson, D.G.; Kjarsgaard, B.A.; Petts, D.C.; Jackson, S.E. Olivine xenocrysts reveal carbonated mid-lithosphere in the northern Slave craton. *Lithos* **2022**, *414*, 106633. [CrossRef]

44. Moore, A.; Costin, G.; Proyer, A. Cognate versus xenocrystic olivines in kimberlites—A review. *Earth Sci. Rev.* **2021**, *221*, 103771. [CrossRef]

45. Xing, C.M.; Wang, C.Y.; Charlier, B.; Namur, O. Ubiquitous dendritic olivine constructs initial crystal framework of mafic magma chamber. *Earth Planet Sci. Lett.* **2022**, *594*, 117710. [CrossRef]

46. Li, D.; Wu, Z.; Sun, X.; Shuai, S.; Fu, Y.; Li, D.; Chen, H.; Lu, Y.; Hong, L. Emplacement ages of diamondiferous kimberlites in the Wafangdian District, North China Craton: New evidence from LA-ICP-MS U-Pb geochronology of andradite-rich garnet. *Gondwana Res.* **2022**, *109*, 493–517. [CrossRef]

47. Dawson, J.B.; Smith, J.V. Chemistry and origin of phlogopite megacrysts in kimberlite. *Nature* **1975**, *253*, 336–338. [CrossRef]

48. Foley, S. Vein-plus-wall-rock melting mechanisms in the lithosphere and the origin of potassic alkaline magmas. *Lithos* **1992**, *28*, 435–453. [CrossRef]

49. Van Achterbergh, E.; Griffn, W.L.; Stiefenhofer, J. Metasomatism in mantle xenoliths from the Letlhakane kimberlites: Estimation of element fluxes. *Contrib Miner. Petrol.* **2001**, *141*, 397–414. [CrossRef]

50. Grégoire, M.; Bell, D.; Le Roex, A. Trace element geochemistry of phlogopite-rich mafic mantle xenoliths: Their classification and their relationship to phlogopite-bearing peridotites and kimberlites revisited. *Contrib. Mineral. Petrol.* **2002**, *142*, 603–625. [CrossRef]

51. Grégoire, M.; Rabinowicz, M.; Janse, A.J.A. Mantle mush compaction: A key to understand the mechanisms of concentration of kimberlite melts and initiation of swarms of kimberlite dykes. *J. Petrol.* **2006**, *47*, 631–646. [CrossRef]

52. O'Reilly, S.Y.; Griffin, W.L. Mantle metasomatism. In *Lecture Notes in Earth System Sciences*; Harlov, D.E., Håkon, A., Eds.; Springer International Publishing: Berlin/Heidelberg, Germany, 2013; pp. 471–533. [CrossRef]

53. Safonov, O.G.; Butvina, V.G. Indicator reactions of K and Na activities in the upper mantle: Natural mineral assemblages, experimental data, and thermodynamic modeling. *Geochem. Int.* **2016**, *54*, 858–872. [CrossRef]

54. Kargin, A.V.; Sazonova, L.V.; Nosova, A.A.; Lebedeva, N.M.; Tretyachenko, V.V.; Abersteiner, A. Cr-rich clinopyroxene megacrysts from the Grib kimberlite, Arkhangelsk province, Russia: Relation to clinopyroxene–phlogopite xenoliths and evidence for mantle metasomatism by kimberlite melts. *Lithos* **2017**, *292–293*, 34–48. [CrossRef]

55. Fu, H.T.; Wan, F.L.; Jiang, L.L.; Xu, H.; Li, Y.X.; Yang, L. Geological Characteristics of Kimberlites in Wafangdian Diamond Orefield, Liaoning Province. *Acta Geosci. Sin.* **2021**, *42*, 859–867. [CrossRef]

56. Thompson, J.M.; Meffre, S.; Danyushevsky, L. Impact of air, laser pulse width and fluence on U-Pb dating of zircons by LA-ICPMS. *J. Anal. At. Spectrom.* **2018**, *33*, 221–230. [CrossRef]

57. Paton, C.; Hellstrom, J.; Paul, B.; Woodhead, J.; Hergt, J. Iolite: Freeware for the visualisation and processing of mass spectrometric data. *J. Anal. At. Spectrom.* **2011**, *26*, 2508–2518. [CrossRef]

58. Wang, S.; Zhang, J.; Han, S.; Wang, J. Petrography and petrogenesis of porphyritic kimberlite from South Liaoning. *Acta Geol. Sin.* **2020**, *94*, 2677–2686.

59. Giuliani, A.; Phillips, D.; Kamenetsky, V.S.; Kendrick, M.A.; Wyatt, B.A.; Goemann, K.; Hutchinson, G. Petrogenesis of mantle polymict breccias: Insights into mantle processes coeval with kimberlite magmatism. *J. Petrol.* **2014**, *55*, 831–858. [CrossRef]

60. Arndt, N.T.; Guitreau, M.; Boullier, A.M.; Le Roex, A.; Tommasi, A.; Cordier, P.; Sobolev, A. Olivine, and the origin of kimberlite. *J. Petrol.* **2010**, *51*, 573–602. [CrossRef]

61. Pilbeam, L.H.; Nielsen, T.F.D.; Waight, T.E. Digestion fractional crystallization (DFC): An important process in the genesis of kimberlites. Evidence from olivine in the Majuagaa kimberlite, Southern West Greenland. *J. Petrol.* **2013**, *54*, 1399–1425. [CrossRef]

62. Schulze, D.J. Origins of chromian and aluminous spinel macrocrysts from kimberlites in southern africa. *Can. Mineral.* **2001**, *39*, 361–376. [CrossRef]

63. Kargin, A.V.; Sazonova, L.V.; Nosova, A.A.; Lebedeva, N.M.; Kostitsyn, Y.A. Phlogopite in mantle xenoliths and kimberlite from the Grib pipe, Arkhangelsk province, Russia: Evidence for multi-stage mantlemetasomatism and origin of phlogopite in kimberlite. *Geosci. Front.* **2019**, *10*, 1941–1959. [CrossRef]

64. Wyllie, P.J. The origin of kimberlite. *J. Geophys. Res.* **1980**, *85*, 6902–6910. [CrossRef]

65. Farmer, G.L.; Boettcher, A.L. Petrologic and crystal-chemical significance of some deep-seated phlogopitesl. *Am. Mineral.* **1981**, *66*, 1154–1163.

66. Griffin, W.L.; Shee, S.R.; Ryan, C.G.; Win, T.T.; Wyatt, B.A. Harzburgite to Iherzolite and back again: Metasomatic processes in ultramafic xenoliths from the Wesselton kimberlite, Kimberley, South Africa. *Contrib. Mineral. Petrol.* **1999**, *134*, 232–250. [CrossRef]

67. Beard, A.D.; Downes, H.; Hegner, E.; Sablukov, S.M. Geochemistry and mineralogy of kimberlites from the Arkhangelsk Region, NW Russia: Evidence for transitional kimberlite magma types. *Lithos* **2000**, *51*, 47–73. [CrossRef]

68. Howarth, G.H.; Giuliani, A. Contrasting types of micaceous kimberlite-lamproite magmatism from the Man Craton (West Africa): New insights from petrography and mineral chemistry. *Lithos* **2020**, *362*, 105483. [CrossRef]

69. Xiang, Z.; Yang, Z.; Lei, X. The microfabrics of phlogopite from the mengyin kimberlites and their implications to the magma evolution. *Bull. Mineral. Petrol. Geochem.* **2020**, *39*, 105–115. [CrossRef]

70. Fedortchouk, Y.; Canil, D. Intensive variables in kimberlite magmas, Lac de Gras, Canada and implications for diamond survival. *J. Petrol.* **2004**, *45*, 1725–1745. [CrossRef]

71. Smith, J.V.; Brennesholtz, R.; Dawson, J.B. Chemistry of micas from kimberlites and xenoliths-I. Micaceous kimberlites. *Geochim. Cosmochim. Acta* **1978**, *42*, 959–971. [CrossRef]

72. Bussweiler, Y.; Foley, S.F.; Prelević, D.; Jacob, D.E. The olivine macrocryst problem: New insights from minor and trace element compositions of olivine from Lac de Gras kimberlites, Canada. *Lithos* **2015**, *220–223*, 238–252. [CrossRef]

73. Lim, E.; Giuliani, A.; Phillips, D.; Goemann, K. Origin of complex zoning in olivine from diverse, diamondiferous kimberlites and tectonic settings: Ekati (Canada), Alto Paranaiba (Brazil) and Kaalvallei (South Africa). *Miner. Pet.* **2018**, *112*, 539–554. [CrossRef]

74. Edgar, A.D.; Arima, M. Conditions of phlogopite crystallization in ultrapotassic volcanic rocks. *Miner. Mag.* **1983**, *47*, 11–19. [CrossRef]

75. Beard, A.D.; Downes, H.; Hegner, E.; Sablukov, S.M.; Vetrin, V.R.; Balogh, K. Mineralogy and geochemistry of Devonian ultramafic minor intrusions of the southern Kola Peninsula, Russia: Implications for the petrogenesis of kimberlites and melilitites. *Contrib. Miner. Petrol.* **1998**, *130*, 288–303. [CrossRef]

76. Gaspar, J.C.; Wyllie, P.J. Barium phlogopite from the Jacupiranga carbonatite, Brazil. *Am. Mineral.* **1982**, *67*, 997–1000.

77. Shaikh, A.M.; Kumar, S.P.; Patel, S.C.; Thakur, S.S.; Ravi, S.; Behera, D. The P3 kimberlite and P4 lamproite, Wajrakarur kimberlite field, India: Mineralogy, and major and minor element compositions of olivines as records of their phenocrystic vs. xenocrystic origin. *Miner. Pet.* **2018**, *112*, 609–624. [CrossRef]

78. Chepurov, A.I.; Zhimulev, E.I.; Agafonov, L.V.; Sonin, V.M.; Chepurov, A.A.; Tomilenko, A.A. The stability of ortho- and clinopyroxenes, olivine, and garnet in kimberlitic magma. *Russ. Geol. Geophys.* **2013**, *54*, 406–415. [CrossRef]

79. Kamenetsky, V.S.; Yaxley, G.M. Carbonate-silicate liquid immiscibility in the mantle propels kimberlite magma ascent. *Geochim. Cosmochim. Acta* **2015**, *158*, 48–56. [CrossRef]

80. Kamenetsky, V.S.; Kamenetsky, M.B.; Sobolev, A.V.; Golovin, A.V.; Sharygin, V.V.; Pokhilenko, N.P.; Sobolev, N.V. Can pyroxenes be liquidus minerals in the kimberlite magma? *Lithos* **2009**, *112*, 213–222. [CrossRef]

81. Mitchell, R.H. Petrology of hypabyssal kimberlites: Relevance to primary magma compositions. *J. Volcanol. Geotherm. Res.* **2008**, *174*, 1–8. [CrossRef]

82. Canil, D.; Fedortchouk, Y. Garnet dissolution and the emplacement of kimberlites. *Earth Planet Sci. Lett.* **1999**, *167*, 227–237. [CrossRef]